J. Fluid Mech. (2000), *vol.* 402, *pp.* 1–32. Printed in the United Kingdom

Numerical studies of two-dimensional Faraday oscillations of inviscid fluids

By JEFF WRIGHT, STEVE YON AND C. POZRIKIDIS†

University of California, San Diego, La Jolla, CA 92093-0411, USA

(Received 19 November 1998 and in revised form 20 July 1999)

The dynamics of two-dimensional standing periodic waves at the interface between two inviscid fluids with different densities, subject to monochromatic oscillations normal to the unperturbed interface, is studied under normal- and low-gravity conditions. The motion is simulated over an extended period of time, or up to the point where the interface intersects itself or the curvature becomes very large, using two numerical methods: a boundary-integral method that is applicable when the density of one fluid is negligible compared to that of the other, and a vortex-sheet method that is applicable to the more general case of arbitrary densities. The numerical procedure for the boundary-integral formulation uses a global isoparametric parametrization based on cubic splines, whereas the numerical method for the vortex-sheet formulation uses a local boundary-element parametrization based on circular arcs. Viscous dissipation is simulated by means of a phenomenological damping coefficient added to the Bernoulli equation or to the evolution equation for the strength of the vortex sheet. A comparative study reveals that the boundary-integral method is generally more accurate for simulating the motion over an extended period of time, but the vortex-sheet formulation is significantly more efficient. In the limit of small deformations, the numerical results are in excellent agreement with those predicted by the linear model expressed by Mathieu's equation, and are consistent with the predictions of the Floquet stability analysis. Nonlinear effects for non-infinitesimal amplitudes are manifested in several ways: deviation from the predictions of Mathieu's equation, especially at the extremes of the interfacial oscillation; growth of harmonic waves with wavenumbers in the unstable regimes of the Mathieu stability diagram; formation of complex interfacial structures including paired travelling waves; entrainment and mixing by ejection of droplets from one fluid into the other; and the temporal period tripling observed recently by Jiang *et al.* (1998). Case studies show that the surface tension, density ratio, and magnitude of forcing play a significant role in determining the dynamics of the developing interfacial patterns.

1. Introduction

The response of a fluid interface to a generally time-dependent body force or, equivalently, to an externally imposed time-dependent acceleration, warrants attention for two reasons. First, it is relevant to a broad range of natural phenomena and engineering applications involving fluid mixing and liquid sloshing due to agitation or container motion. Second, it provides us with a well-defined system for studying the nonlinear dynamics of interfacial motion in two-phase flow. Three special protocols

† Corresponding author: e-mail: cpozrikidis@ucsd.edu

of acceleration normal to an interface have received special attention: a constant acceleration associated with the Rayleigh–Taylor instability; an impulsive acceleration associated with the Richtmyer–Meshkov instability; and a harmonic acceleration, possibly in the presence of a constant body force, associated with Faraday waves. In this paper, we consider the third type of motion.

The dynamics of an interface under the influence of a harmonic acceleration has been the subject of numerous experimental and theoretical investigations dating back to Faraday's observations in 1831, as reviewed by Miles & Henderson (1990). Recent experimental studies confirmed that a harmonically forced system may sustain finite-amplitude waves over a broad range of frequencies and amplitudes of the container motion (e.g. Edwards & Fauve 1994; Kudrolli & Gollub 1996*a*, *b*). The spatial form and temporal evolution of these waves are affected by the geometry of the container, the viscosity of the fluids, and the behaviour of the contact angle or motion of the contact line. Under most conditions, the waves have a square pattern and oscillate at half the frequency of the external acceleration with a modulated amplitude. A host of further patterns have been observed, especially for polychromatic accelerations.

Experiments have revealed that as the amplitude of the acceleration is raised, spatially periodic regular patterns with square, hexagonal, and triangular cells yield disordered and fluctuating states (e.g. Crawford, Gollub & Lane 1993). Under certain conditions, soliton-like deformations develop, adding to the diversity of the nonlinear motion (Wu, Keolian & Rudnick 1984; Miles 1984*b*). When the amplitude of the oscillations exceeds a critical threshold, cusped interfacial waves, ejection of droplets, intense mixing, and temporal period tripling arise (Mesquita, Kane & Gollub 1992; Goodrich *et al.* 1997; Jiang *et al.* 1998). Fauve *et al.* (1992), Edwards & Fauve (1993), and Kumar & Bajaj (1995) showed that two-dimensional striped patterns dominate as the effects of viscosity become important.

During a cycle of the oscillation, the fluids on either side of an interface are subjected to stabilizing and destabilizing acceleration directed from the light to the heavy fluid and vice versa. The interplay between the Rayleigh–Taylor instability, prevailing in the first half-cycle of the vibration, and the stabilizing influence of the fluid acceleration directed from the heavy to the light fluid, prevailing in the second half-cycle of the vibration, is responsible for temporal asymmetry of the wave profiles during a complete cycle. This asymmetry should be contrasted with the symmetry of unforced gravity or capillary waves. If the frequency of the oscillation is small, the interface is subjected to destabilizing acceleration for a sufficiently long period of time, and this allows the Rayleigh–Taylor instability to proceed into its nonlinear stages causing the development of spikes and bubbles.

To explain Faraday's observations, Benjamin & Ursell (1954) considered the harmonic oscillation of the free surface of an inviscid liquid of finite depth placed within a cylindrical container underneath another fluid with negligible density, assuming that the contact line meets the container at a right-angle (see also Sorokin 1957). In their analysis, the position of the free surface is described as a weighted sum of eigenfunctions corresponding to the vessel geometry or to the assumed spatial periodicity of the interfacial pattern. Linearization yields a de-coupled system of linear ordinary differential equations governing the evolution of the coefficients of the eigenfunctions, and straightforward rearrangement yields Mathieu's equation. The well-known properties of the solutions of Mathieu's equation, deduced by carrying out a Floquet stability analysis, reveal the existence of regimes where the standing waves are periodic or non-periodic but bounded, and regimes where the amplitude grows at an exponential rate and the flow is unstable (e.g. Abramowitz & Stegun 1964, Chap. 20).

The Floquet stability analysis of Mathieu's equation reveals that, given the fluid densities, the interfacial tension, the amplitude of the acceleration, and the forcing frequency, instability occurs for unstable wavenumbers that fall within separated bands. In laboratory experiments, the wavenumbers most often observed correspond to Faraday waves, that is, to waves whose angular frequency is half the forcing frequency of the external acceleration. Benjamin & Ursell (1954) rationalized this selection by arguing that viscous dissipation favours waves with the smallest possible wavenumbers; these are the waves that oscillate with angular frequency that is equal to half the forcing frequency of the external acceleration, and is closest to the natural frequency of the selected waves.

Skalak & Yarymovych (1960) and Ockendon & Ockendon (1973) developed perturbation expansions for the amplitude of free-surface waves in potential flow, and demonstrated the occurrence of subharmonic frequencies at the third-order expansion. Their studies have been followed by a large number of asymptotic analyses of the weakly nonlinear motion, all up to third or fifth order with respect to the wave amplitude, as reviewed and discussed by Miles (1984*a*, 1993) and Miles & Henderson (1990). The most advanced models are able to describe the wavelength selection and hysteresis observed in the experiments (Craik & Armitage 1995). The highly nonlinear motion of an interface with finite- and large-amplitude deformations has to date not been simulated by numerical methods. An exception is the recent work of Jiang *et al.* (1996) who performed boundary-integral simulations of two-dimensional motion based on Cauchy's integral method, and compared the numerical results of their simulations to their own laboratory observations.

Kumar & Tuckerman (1994) carried out a Floquet analysis taking full account of the viscosities of the fluids. When viscous effects are included, the linearized evolution equations can no longer be reduced to a single ordinary differential equation, and an eigenvalue problem involving partial-differential equations must be solved. In earlier studies, the effect of the viscosity had been emulated by including a damping term in Mathieu's equation or a dissipation term in Bernoulli's equation. The effect of viscosity was discussed by several subsequent authors and more recently by Cerda & Tirapegui (1998) who found that the nature of the instability for slightly viscous fluids is fundamentally different from that for highly viscous fluids, and a Mathieu equation may be derived to describe the dynamics of the free surface in the presence of dominant viscous stresses.

In the present work, we study the fully nonlinear dynamics of forced standing waves at the interface between two semi-infinite inviscid fluids, subject to oscillatory acceleration. The investigations are based on numerical simulations of the two-dimensional motion subject to periodic boundary conditions, in the absence of contact lines. The goal of this study is threefold: first, to illustrate the mechanism by which the growth of small-amplitude perturbations yields nonlinear waves; second, to investigate the significance of the various problem parameters on the nature of the large-amplitude motion; third, to identify regimes where violent interfacial motion leads to strong deformation and interface breakup. For the purpose of comparing the numerical results with laboratory observations, we account for viscous dissipation in the bulk of the fluids in terms of a phenomenological damping coefficient included in the equation of motion.

The simulations are conducted using two numerical methods. The first method is based on the boundary-integral formulation for potential flow, and is applicable when the density of one of the fluids is negligible compared to that of the other. The numerical procedure involves integrating in time the differential equations that

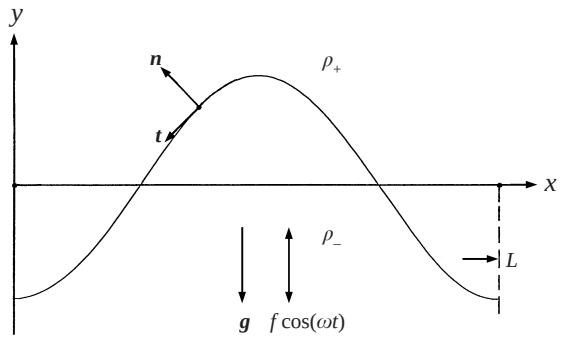

FIGURE 1. Schematic illustration of the initial state of a sinusoidally perturbed interface separating two inviscid fluids.

govern the motion of interfacial marker points and the evolution of the harmonic potential. The second method is based on a representation of the flow in terms of a vortex sheet, and is applicable when the densities of both fluids are non-zero. The numerical procedure involves integrating in time the differential equations that govern the motion of interfacial marker points, and solving an integral equation for the rate of change of the strength of the vortex sheet. Similar methods have been used by several previous investigators to tackle problems of vortex motion and free-surface flow, but a direct comparison has not been made. The dual numerical development serves two purposes: it provides us with a basis for validating the results of the simulations over an extended period of time; and it allows us to compare the relative merits of the two approaches in the more general context of potential flow.

2. Problem statement and formulation

Consider the interface between two incompressible semi-infinite fluids with constant surface tension τ, subject to vertical harmonic acceleration, as illustrated in figure 1. In the undeformed state, the interface is flat and the fluids move like rigid bodies along the y-axis with acceleration $f\exp(-\mathrm{i}\omega t)$, velocity $(\mathrm{i}f/\omega)\exp(-\mathrm{i}\omega t)$, and displacement $d\exp(-\mathrm{i}\omega t)$, where f is the constant amplitude of the acceleration, ω is the angular frequency of the oscillation, and $d=-f/\omega^2$ is the amplitude of the displacement. We are interested in describing the motion of the interface subject to spatially-periodic two-dimensional perturbations in the form of standing waves with wavelength L and wavenumber $k=2\pi/L$, as illustrated in figure 1.

In a frame of reference moving with the unperturbed interface, the imposed acceleration is mediated by an oscillatory body force. When the motion is irrotational, the flow on either side of the interface is described by the modified Euler equation

$$\frac{\partial \boldsymbol{u}_\pm}{\partial t}+\boldsymbol{u}_\pm\cdot\nabla\boldsymbol{u}_\pm=-\frac{\nabla p_\pm}{\rho_\pm}+\boldsymbol{g}-\boldsymbol{e}_y f\cos(\omega t)+\zeta\boldsymbol{u}_\pm \tag{2.1}$$

and the continuity equation

$$\nabla\cdot\boldsymbol{u}_\pm=0, \tag{2.2}$$

where $\boldsymbol{u}$ is the fluid velocity, p is the pressure, $\boldsymbol{g}$ is the acceleration due to gravity, $\boldsymbol{e}_y$ is the unit vector along the y-axis, and the subscripts $+$ or $-$ indicate, respectively, the upper or lower fluid.

Although the flow has been assumed to be irrotational, with the consequence that

all dynamic boundary conditions cannot be fulfilled at the interface, the rate of viscous dissipation in the bulk of the fluids does not vanish. When the viscosity of one of the fluids is negligible compared to that of the other, the boundary layer along the free surface is weak, and the rate of viscous dissipation within it is much less than that within the bulk of the fluids (e.g. Pozrikidis 1997). In the limit of small-amplitude waves, viscous dissipation causes the amplitude of the interface and the magnitude of the fluid velocity to decay at a rate that is proportional to $2\nu k^2$, where ν is the kinematic viscosity (Landau & Lifshitz 1987, pp. 92–93). In an attempt to phenomenologically emulate the effects of viscosity for both infinitesimal- and finite-amplitude oscillations of a viscous–inviscid interface, and thus to be able to compare the numerical results with laboratory observations, we have included the linear damping term $\zeta \boldsymbol{u}_{\pm}$ on the right-hand side of equation (2.1), where ζ is a phenomenological damping coefficient. Jiang *et al.* (1998) also included this term in the Euler equation to obtain agreement with their laboratory observations. Previous linear and weakly non-linear analyses provide evidence that the phenomenological dissipation term correctly accounts for the weak effects of viscosity; that is, it is physically relevant at high Reynolds numbers (e.g. Kumar & Tuckerman 1994; Edwards & Fauve 1993; Cerda & Tirapegui 1998).

In a frame of reference moving with the unperturbed interface, the velocity is required to vanish far above and below the interface. The normal component of the fluid velocity is required to be continuous across the interface, but the tangential component may suffer a discontinuity which amounts to an interfacial vortex sheet. This interpretation provides a basis for representing the vortex sheet discussed in the next section.

2.1. *Floquet analysis*

As a prelude to the numerical results, we briefly review the Floquet stability analysis for small two-dimensional interfacial deformations. Following Benjamin & Ursell (1954), we describe the position of the interface in the form $y = a(t)\exp(\mathrm{i}kx)$, and linearize the governing equations and interfacial conditions to derive the modified Mathieu equation

$$\frac{\mathrm{d}^2 a}{\mathrm{d}\hat{t}^2} + \delta \frac{\mathrm{d}a}{\mathrm{d}\hat{t}} + [p - 2q\cos(2\hat{t})]a = 0 \tag{2.3}$$

with a linear resistive term included, where $\hat{t} = \omega t/2$, is the dimensionless time. We have introduced the parameters

$$p = \left(\frac{2\omega_n(k)}{\omega}\right)^2, \quad q = 2\frac{kf}{\omega^2}A, \quad \delta = \frac{2\zeta}{\omega}, \quad \omega_n^2(k) = \frac{kg}{\omega^2}\left(A + \frac{\tau k^2}{g(\rho_- + \rho_+)}\right), \tag{2.4}$$

where $\omega_n(k)$ is the wavenumber dependent natural angular frequency of unforced gravity–capillary standing waves, and

$$A = \frac{\rho_- - \rho_+}{\rho_- + \rho_+} \tag{2.5}$$

is the Atwood ratio.

We note that the term $p - 2q\cos(2\hat{t})$ in equation (2.3) is periodic with period π, and search for particular solutions in the form

$$a(\hat{t}) = P(\hat{t})\exp(-\mathrm{i}\sigma\hat{t}), \tag{2.6}$$

where i is the imaginary unit, $P(\hat{t})$ is a periodic function with period π, and σ is the characteristic or Floquet exponent (e.g. Coddington & Levinson 1955, Chap. 8;

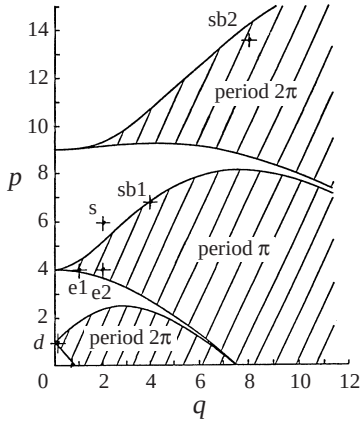

FIGURE 2. The stability diagram for the Mathieu equation. In the hatched regions, the amplitude of the interface grows exponentially at a rate that is equal to the imaginary part of the Floquet exponent. In the unhatched regions, the amplitude is oscillatory but not periodic. The points labelled 's', 'sb1' etc. correspond to the numerical results discussed in § 4.

Jordan & Smith 1987, Chap. 9). Expressing $P(\hat{t})$ in the form

$$P(\hat{t}) = \sum_{m=-\infty}^{\infty} c_{2m} \exp(-\mathrm{i}2m\hat{t}) \tag{2.7}$$

and substituting equations (2.6) and (2.7) into equation (2.3), we obtain

$$\sum_{m=-\infty}^{\infty} \{-(2m+\sigma)^2 - \mathrm{i}\delta(2m+\sigma) + p - q(\mathrm{e}^{\mathrm{i}2\hat{t}} + \mathrm{e}^{-\mathrm{i}2\hat{t}})\}\mathrm{e}^{-\mathrm{i}(2m+\sigma)2\hat{t}} c_{2m} = 0. \tag{2.8}$$

Collecting factors with same exponential terms, we derive the following infinite system of homogeneous linear equations for the coefficients c_{2m}:

$$-q\, c_{2m-2} + [p - (2m+\sigma_r)^2 + \sigma_i^2 + \delta\sigma_i - \mathrm{i}(2\sigma_i + \delta)(2m+\sigma_r)]c_{2m} - q\, c_{2m+2} = 0. \tag{2.9}$$

For arbitrary values of p, q, and δ, the real and imaginary parts of the characteristic exponent, σ_r and σ_i, may be obtained by setting the determinant of the following tridiagonal matrix equal to zero:

$$\begin{bmatrix} \ddots & -q & 0 \\ -q & p - \sigma_r^2 + \sigma_i^2 + \delta\sigma_i - \mathrm{i}(2\sigma_i + \delta)\sigma_r & -q \\ 0 & -q & \ddots \end{bmatrix}, \tag{2.10}$$

and then solving the resulting nonlinear eigenvalue problem using a numerical method. The numerical error introduced by truncation is discussed by Wright (1999). For a certain value of δ, an infinite number of characteristic exponents exist for each combination of p and q, but the functional form of the coefficients in (2.9) ensures that any two exponents will differ by the constant $\pm 2l$, where l is an integer. Since the imaginary parts of the characteristic exponents are identical, all components of the particular solutions $a(\hat{t})$ grow or decay at the same exponential rate while oscillating with different angular frequencies.

When $\delta = 0$, equation (2.3) reduces to the standard Mathieu equation. In this case, the Floquet analysis reveals regimes of periodic solutions, regimes where the solution

is oscillatory but not periodic, and regimes where the amplitude of the interface grows at an exponential rate leading to unstable motion (e.g. Abramowitz & Stegun 1972, Chap. 20). The stability boundaries for the Mathieu equation are reproduced in figure 2 for future reference. In the shades areas labelled 'period 2π', the real part of the Floquet exponent is an odd integer; in the shades area labelled 'period π', the real part of the Floquet exponent is an even integer. Note that for small forcing amplitudes, corresponding to small values of q, instability first occurs when p is on the order of unity, in which case the forcing frequency is comparable to the natural frequency of the selected wave.

When $\delta > 0$, the stability boundaries are shifted in a smooth fashion to restrict the range of unstable wavenumbers, as discussed by Kumar & Tuckerman (1994), Cerda & Tirapegui (1998), and Wright (1999). It should be emphasized, however, that the phenomenological correction expressed by δ is consistent with the linearized theory only when one of the fluids is inviscid; otherwise, the shear stress at the interface is non-zero, and the viscous dissipation within the boundary layer established along the interface is comparable to that within the bulk of the fluids. Kumar & Tuckerman (1994) found that the stability thresholds predicted by the Floquet analysis of equation (2.3) grossly underestimate those that arise by carrying out a Floquet analysis of the unsimplified Navier–Stokes equation.

Wright (1999) discusses an alternative method of computing the Floquet exponents of the Mathieu equation that is applicable to a broader range of problems. The idea is to generate a time series by solving the governing equation using a numerical method subject to an arbitrary initial condition, in this case the Mathieu equation, and then approximate the time series with a finite sum of complex exponentials in time using Prony's method of exponential fitting (Pozrikidis 1998*b*, 1999*a*). The complex coefficients that multiply time in the exponents are approximations to the Floquet exponents. The method can be rationalized by observing that fitting with a finite sum is equivalent to truncating the Floquet expansion (2.7) to a certain level, which is reasonable as long as the magnitude of the complex coefficients decays at a sufficiently high rate. In practice, it is found that unless the number of terms in the series is sufficiently large, the error due to the truncation is substantial, and the method of Prony fitting is inferior to the matrix method discussed in a previous paragraph.

3. Numerical methods

To study the nonlinear dynamics of the interfacial waves, we carry out numerical simulations using two independent numerical methods that are discussed, validated, and compared in this section.

3.1. *Boundary integral formulation*

When the density of the upper fluid is negligible, the pressure on the upper side of the interface is constant, and the evolution of the interface is determined by the motion of the lower fluid alone. Assuming that the flow is irrotational, we introduce the harmonic velocity potential ϕ so that $\boldsymbol{u} = \nabla\phi$ in the lower fluid, and develop an integral equation that relates the distribution of ϕ and its normal derivative $\boldsymbol{n}\cdot\nabla\phi$ along the free surface.

We adopt the formulation of Longuet-Higgins & Cokelet (1976), and introduce the physical and image complex planes with complex variables $z = x + \mathrm{i}y$ and $\hat{z} = \hat{x} + \mathrm{i}\hat{y}$, and the coordinate transformation $\hat{z} = \exp(-\mathrm{i}2\pi z/L)$ that maps one period of the

interface in the physical plane, denoted as I, onto a closed contour C in the image plane. Since the transformation is conformal, and since the potential is single-valued everywhere within the closed contour due to the periodicity of the flow and the requirement that the potential must vanish far below the free surface, the potential remains harmonic in the transformed plane; that is, ϕ is a harmonic function of $\hat{x}$ and $\hat{y}$. The velocity in the (x, y)-plane is related to the velocity in the $(\hat{x}, \hat{y})$-plane by expressions that arise by applying the chain rule; the final forms involve, for example, the coordinate derivative $\partial\hat{x}/\partial y$. Green's third identity in the image plane provides us with the integral equation

$$\phi(\hat{x}_0) = -\frac{1}{\pi}\int_C \ln r \ \nabla\phi\cdot\boldsymbol{n}\,\mathrm{d}l + \frac{1}{\pi}\int_C^{\mathrm{PV}} \phi \ \nabla \ \ln r\cdot\boldsymbol{n}\,\mathrm{d}l, \tag{3.1}$$

where the point $\hat{x}_0$ lies on C, $r = |\hat{\boldsymbol{x}} - \hat{\boldsymbol{x}}_0|$, and PV denotes the principal value of the double-layer harmonic potential (e.g. Pozrikidis 1997).

In the numerical procedure, one period of the free surface is traced by a set of N marker points, and values of the potential are assigned at the location of the marker points. Typically, the initial potential is set equal to zero at all marker points. One period of the interface in the physical plane is mapped to a closed boundary in the $(\hat{x}, \hat{y})$-plane using the aforementioned conformal mapping, and the integral equation (3.1) is solved for the normal derivative of the potential over the closed contour in the $(\hat{x}, \hat{y})$-plane, as will be discussed in the next paragraph. The tangential derivative of the potential is computed by numerical differentiation using cubic-spline interpolation with respect to the polygonal arclength. The normal and tangential spatial derivatives of the potential are then transformed back to the physical plane to yield the corresponding components of the fluid velocity. The rate of change of the potential following a point particle over the physical interface is subsequently computed using Bernoulli's equation

$$\frac{\mathrm{D}\phi}{\mathrm{D}t} = -\frac{p}{\rho} + \frac{1}{2}\boldsymbol{u}\cdot\boldsymbol{u} - y(g + f\cos(\omega t)) - \zeta\phi, \tag{3.2}$$

where $\mathrm{D}/\mathrm{D}t$ is the material derivative, $p = p_0 + \tau\kappa$ is the pressure in the fluid at the free surface, p_0 is the constant pressure above the free surface, and κ is the curvature of the free surface in the (x, y)-plane. The potential and position of the marker points are updated in time by the second-order Runge–Kutta method. When the inverse Weber number $\Gamma = \tau k^3/\omega^2\rho_-$ is large, the position of the marker points and potential are smoothed after a certain number of steps using the five-point formula of Longuet-Higgins & Cokelet (1976).

To solve the integral equation (3.1) for the normal derivative of potential in the image plane, the distribution of the potential and the Cartesian coordinates of marker points along the closed boundary are approximated using cubic splines with respect to the polygonal arclength with periodic end conditions. Although computationally involved, the high-order accuracy associated with the cubic splines is crucial to the performance of the numerical method for long simulation times. To obtain the matrix of coefficients for the unknown values of $\boldsymbol{n}\cdot\nabla\phi$ at the location of the marker points, the single-layer integral on the left-hand side of equation (3.2) is evaluated by the method of impulses. For a specified image of a marker point $\hat{\boldsymbol{x}}_0$, the value $\boldsymbol{n}\cdot\nabla\phi = 1$ is assigned to a particular marker point while the value $\boldsymbol{n}\cdot\nabla\phi = 0$ is assigned to the remaining marker points, and periodic cubic-spline interpolation is invoked to obtain a continuous and differentiable distribution of the normal derivative of potential over the closed image of the free surface. The single-layer integral is computed using a

combination of the five-point Gauss–Legendre quadrature for the regular elements not containing the singular point $\hat{\boldsymbol{x}}_0$, and the log-singularity Gauss quadrature applied to the singular elements containing the point $\hat{\boldsymbol{x}}_0$ (e.g. Pozrikidis 1998*a*). Scanning the point $\hat{\boldsymbol{x}}_0$, and the marker point at which $\boldsymbol{n}\cdot\nabla\phi = 1$ over the N marker points, we obtain a system of N linear equations for the unknown normal derivatives of the potential at the marker points. The right-hand side of the linear system contains the values of the double-layer integral evaluated at the marker points.

The accurate computation of the double-layer potential is imperative for the reliability of the simulations at long times. In two dimensions, the kernel of the principal value of the harmonic double-layer integral suffers a discontinuity across the singular point and may seemingly be computed with adequate accuracy by integrating separately on either side of the singular point. Numerical experimentation, however, showed that the most accurate results are obtained by expressing the potential in the form

$$\int_C^{\mathrm{PV}} \phi\ \boldsymbol{n}\cdot\nabla \ln r\,\mathrm{d}l\ =\ \int_C (\phi - \phi(\hat{\boldsymbol{x}}_0))\boldsymbol{n}\cdot\nabla\ \ln\ r\ \mathrm{d}l + \pi\ \phi(\hat{\boldsymbol{x}}_0). \tag{3.3}$$

The integral on the right-hand side is computed using the five-point Gauss–Legendre quadrature on the cubic elements that describe the interface between consecutive marker points.

To ensure the adequate resolution of regions of high curvature, the marker points are redistributed after each time step using the method described by Kwak & Pozrikidis (1998). Points are added at regions of high curvature, or when convection has caused the arclength between two successive points to increase beyond a specified threshold. Points are removed from regions of high grid density, provided that the removal does not produce a distribution that violates the aforementioned criteria for point addition based on boundary curvature or maximum point separation.

3.2. *Formulation in terms of an interfacial vortex sheet*

To describe the motion of the interface when the density of the upper fluid is not negligible compared to that of the lower fluid, we regard the flow as being induced by a vortex sheet situated over the interface. The strength of the vortex sheet is equal to the discontinuity in the velocity across the interface, given by $\gamma = (\boldsymbol{u}_+ - \boldsymbol{u}_-)\cdot\boldsymbol{t}$, where $\boldsymbol{t}$ is the unit vector tangent to the interface, oriented as shown in figure 1. The vortex-sheet representation is tantamount to a dipole representation, where the non-periodic strength of the dipoles is equal to the circulation integral along the vortex sheet (Baker, Meiron & Orszag 1982).

As a first step, one period of the interface is described in parametric form in terms of the label a. Taking advantage of the periodicity of the flow, we find that the velocity at a marker point that is located at the interface is given by

$$\boldsymbol{U}(a) = \frac{1}{2L}\int_I^{\mathrm{PV}} \boldsymbol{K}^P(a,a')\ \gamma(a')\,\mathrm{d}a' + (\alpha - \tfrac{1}{2})\,\gamma(a)\,\boldsymbol{t}(a), \tag{3.4}$$

where

$$\boldsymbol{K}^P(a,a') = [\cosh k(y(a)-y(a')) - \cos k(x(a)-x(a'))]^{-1} \begin{bmatrix} -\sinh k(y(a)-y(a')) \\ \sin\ k(x(a)-x(a')) \end{bmatrix} \tag{3.5}$$

is the periodic vortex-sheet kernel, and PV denotes the principal value of the vortex-sheet integral (e.g. Pozrikidis 1997). The arbitrary numerical parameter α on the

right-hand side of (3.4) relates the velocity of the interfacial marker points to the velocity in the upper and lower fluids at the interface. When $\alpha = 0$ or 1, the marker points move with the velocity of the fluid on the upper or lower side of the interface, whereas when $\alpha = \frac{1}{2}$, the marker points move with the principal velocity of the vortex sheet. The significance of this parameter will be discussed later in this section.

The evolution of the strength of the vortex sheet following the marker points is given by the equation

$$\left(\frac{\partial \gamma}{\partial t}\right)_a = \frac{A}{L}\boldsymbol{t}(a)\cdot \int_I^{\mathrm{PV}} \boldsymbol{K}^P(a,a')\left(\frac{\partial \gamma}{\partial t}\right)_{a'} \mathrm{d}a' + F(a), \tag{3.6}$$

where the forcing function $F(a)$ is given by

$$F(a) = -\frac{1}{A_1}\gamma\, \boldsymbol{t}\cdot\frac{\partial \boldsymbol{U}}{\partial l} + 2A\, J(a) + A_2\gamma\, \frac{\partial \gamma}{\partial l} + \frac{2\tau}{\rho_+ + \rho_-}\frac{\partial \kappa}{\partial l} - 2A\, (\boldsymbol{g} - \boldsymbol{e}_y f\, \cos\omega t)\cdot \boldsymbol{t} - 2\zeta\gamma \tag{3.7}$$

and

$$J(a) = \frac{1}{2L}\boldsymbol{t}(a)\cdot \int_I^{\mathrm{PV}} \frac{\partial}{\partial t}(\boldsymbol{K}^P(a,a')_{a,a'})\, \gamma(a')\, \mathrm{d}a' \tag{3.8}$$

(e.g. Pozrikidis 1997). We have introduced the physico-numerical constants

$$A_1 = \frac{1}{2}\frac{\rho_- + \rho_+}{\rho_+ + \alpha(\rho_- - \rho_+)}, \quad A_2 = 2\frac{\rho_-\alpha^2 - \rho_+(1-\alpha^2)}{\rho_- + \rho_+}. \tag{3.9}$$

The last term on the right-hand side of equation (3.7) corresponds to the phenomenological viscous dissipation term in the modified Euler equation applied at a point on the interface, as discussed in § 2. It is clear that this term causes the strength of the vortex sheet to decay in an exponential manner and thus simulates viscous dissipation, but does not necessarily account for the growth of boundary layers along the interface in any rational way.

When the Atwood ratio A defined in equation (2.5) is non-zero, equations (3.6)–(3.9) provide us with a Fredholm integral equation of the second kind for the rate of change of the strength of the vortex sheet following the interfacial marker points. Baker *et al.* (1982) showed, and our numerical computations confirmed, that the integral operator has a globally convergent Neumann series, and the integral equation may be solved by the method of Neumann iterations or successive substitutions. Wright (1999) discusses in detail the spectral radius of the integral operator in terms of the geometry of a periodic vortex sheet. When $A = 0$, the first term on the right-hand side of equation (3.6) and the penultimate term on the right-hand side of (3.7) disappear yielding an explicit expression for the rate of change of the strength of the vortex sheet.

The numerical task is to compute the evolution of the interface using equation (3.4) while simultaneously updating the strength of the vortex sheet by solving the integral equation. Our numerical method follows the general principles of boundary-element methods and is thus an improvement over traditional methods based on the point-vortex approximation (e.g. Puckett 1993). A similar boundary-element method was used by Higdon & Pozrikidis (1985) to compute the evolution of a vortex sheet embedded in a homogeneous fluid corresponding to $A = 0$ in the absence of surface tension. In their case, the circulation along the vortex sheet was conserved at the position of the marker points and the strength of the vortex sheet arose by simple differentiation.

In the numerical method, one period of the vortex sheet is traced with a collection

of N marker points, and initial values for the strength of the vortex sheet are assigned at the marker points. The shape of the vortex sheet is approximated by a collection of blended circular arcs defined in terms of the marker points. The computation of the blended arcs is described in detail by Wright (1999). The tangential vector and curvature of the vortex sheet follow readily from the arc representation. The right-hand side of equation (3.8) is evaluated by integrating over the collection of the individual arcs. To accurately compute the principal-value integral over an arc, we write

$$\int_{\mathrm{Arc}}^{\mathrm{PV}} \boldsymbol{K}^P(a,a')\,\gamma(a')\,\frac{\partial l}{\partial a'}\,\mathrm{d}a' = \int_{\mathrm{Arc}} (\boldsymbol{K}^P-\boldsymbol{K})(a,a')\,\gamma(a')\,\frac{\partial l}{\partial a'}\,\mathrm{d}a' + \int_{\mathrm{Arc}}^{\mathrm{PV}} \boldsymbol{K}(a,a')\,\gamma(a')\,\frac{\partial l}{\partial a'}\,\mathrm{d}a', \tag{3.10}$$

where $\boldsymbol{K}$ is the non-periodic vortex-sheet kernel given by

$$\boldsymbol{K}(a,a') = \frac{1}{[x(a)-x(a')]^2+[y(a)-y(a')]^2}\begin{bmatrix} -y(a)+y(a') \\ x(a)-x(a') \end{bmatrix}, \tag{3.11}$$

and evaluate the first integral on the right-hand side numerically using the Gauss–Legendre quadrature. For the purpose of computing the principal-value integral on the right-hand side of (3.10), we assume that the strength of the vortex sheet varies linearly with respect to the sine of the polar angle that is subtended from the canters of the blended arc centres, measured from an end point. The round-off error due to computation of the inverse trigonometric functions is drastically reduced by integrating in local triangle coordinates, as discussed by Wright (1999).

The rate of change of the strength of the vortex sheet is computed by solving the integral equation using the method of successive substitutions. The iterations are terminated when the change in the vortex sheet strength is less than a specified threshold at each marker point. The function $J(a)$ defined in (3.8) expresses the rate of change of γ following the vortex sheet, computed as though the strength of the vortex sheet remained constant in time. To evaluate this term, we exchange the order of the differential and integral operators, and then perform numerical differentiation using a very small time step. Derivatives with respect to arclength along the interface are evaluated with second-order centred finite differences. After each step, the marker point positions, velocities, and strength of the vortex sheet are regularized using the five-point polynomial smoothing method of Longuet-Higgins & Cokelet (1976), and the marker points are redistributed along the sheet as described in the preceding subsection.

A theory for the optimal choice of the numerical parameter α on the right-hand side of equation (3.8) is not available. Roberts (1983) studied the point-vortex approximation, and found that choosing α so that the point vortices follow one fluid or another prevents the growth of the familiar 'sawtooth' instabilities. Unfortunately, his conclusions are specific to the point-vortex approximation and do not apply to the boundary-element method developed in this work. In a study of singularity formation during the Rayleigh–Taylor instability, Baker, Caflisch & Siegel (1993) argued, on the basis of linear stability analysis, that setting $\alpha = (A+1)/2$ eliminates the dispersion of high wavenumbers, and thereby reduces the numerical error. Their best choice coincides with that of Roberts (1983) when the densities of the fluids are matched or the density of one fluid is negligible compared to that of the other, but not under more general conditions. Finally, based on an analogy with the Burgers equation,

Zufiria (1988) suggested that α should be chosen so that the coefficient in front of the term $\gamma\ \partial\gamma/\partial l$ in equation (3.7) vanishes, thereby preventing the development of shocks in the distribution of the strength of the vortex sheet.

It appears from these earlier studies that the optimal value of α depends not only on the unperturbed strength of the vortex sheet, Atwood ratio, and method of discretization, but also on the type of vortex-sheet motion. While criteria such as conservation of circulation following the marker points could be used as guidelines, we have conducted extensive numerical experiments using as a reference results obtained by the boundary-integral method to find that setting $\alpha = \frac{1}{2}$ is, in general, the most appropriate choice (Wright 1999). Accordingly, this value was adopted in all simulations presented in this paper.

3.3. *Code validation and numerical accuracy*

To investigate the relative performance of the boundary-integral and vortex-sheet methods, we conducted several series of parallel simulations. In all cases, the interface is perturbed by a sinusoidal wave of amplitude a_0 and wavelength L, while the distribution of the potential over the interface and strength of the vortex sheet retain their unperturbed zero values. When the initial amplitude of the interface is small, and the pair (p, q) falls within a regime of stable solutions in the Floquet stability diagram shown in figure 2, the amplitude of the interface remains small but the interfacial oscillation is not necessarily periodic in time.

In figure 3, we present the time history of the amplitude of the interface corresponding to the trough of the initial sinusoid, for a disturbance with initial amplitude $a_0/L = 0.001$, over twenty-four periods of oscillation. In this simulation, $p = 6$, $q = 2$, and $\delta = 0$, corresponding to physical conditions: $\rho_+ = 0$, $\rho_- = 1000\,\mathrm{kg\,m^{-3}}$, $L = 1.0\,\mathrm{m}$, $g = 9.81\,\mathrm{m\ s^{-2}}$, $f = 11.494\,\mathrm{m\ s^{-2}}$, $\omega = 6.0092\,\mathrm{s^{-1}}$, and $\zeta = 0$, which are represented by the point labelled '*s*' (stable) in figure 2. The numerical results were obtained using the boundary-integral and the vortex-sheet methods with a fixed number of 60 marker points over each period. In this case, higher harmonics are not excited and the interface remains sinusoidal throughout the simulation. Figure 3(*a*) shows that both methods consistently reproduce the overall features of the solution of Mathieu's equation. Closer examination near the end of the simulation presented in figure 3(*b*), however, reveals that both numerical solutions eventually deviate from the linearized predictions. The difference between the numerical solutions and the linearized prediction is reduced as the number of interfacial marker points is increased, but this results in substantially longer computational time and requires smaller time steps.

Overall, the comparisons shown in figure 3 confirm the consistency of the two numerical methods. Numerical experimentation showed that without using identity (3.3) to compute the double-layer potential, the accuracy of the boundary-integral method is significantly inferior to that of the vortex-sheet method, and this results in discrepancies with the theoretical predictions at earlier times. In contrast, the vortex-sheet method is less sensitive to the accuracy of the intermediate computations. The reason for this behaviour is not entirely clear.

The complete boundary-integral solution shown in figure 3 requires approximately 12 hours of CPU time on a 200 MHz Pentium Pro running LINUX 4.1 and a FORTRAN 77 compiler, while the vortex solution requires only 3 hours. The increased computational time in the first case is due to the formulation in terms of a Fredholm integral equation of the first kind, which requires the solution of a linear system at each time step.

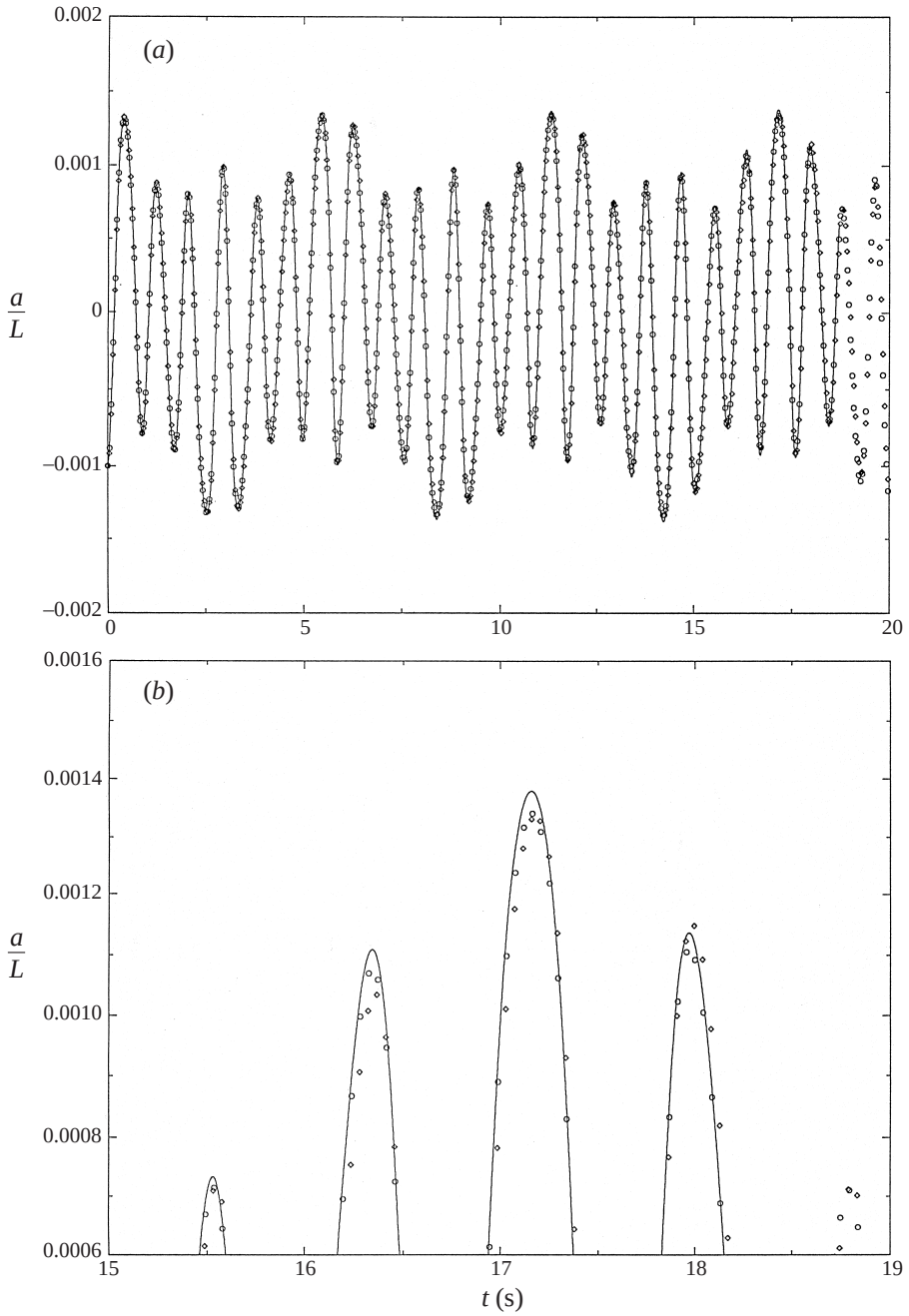

FIGURE 3. Time history of the amplitude of the interface for $p = 6$, $q = 2$, and $a_0/L = 0.001$, represented by the point labelled 's' in figure 2. The solid line represents the solution of the Mathieu equation with $\delta = 0$; the circles and diamonds represent, respectively, solutions obtained with the boundary-integral and vortex formulations. Panel (*b*) is a magnification of the tail-end of (*a*) showing deviation of the numerical results from the Mathieu solution.

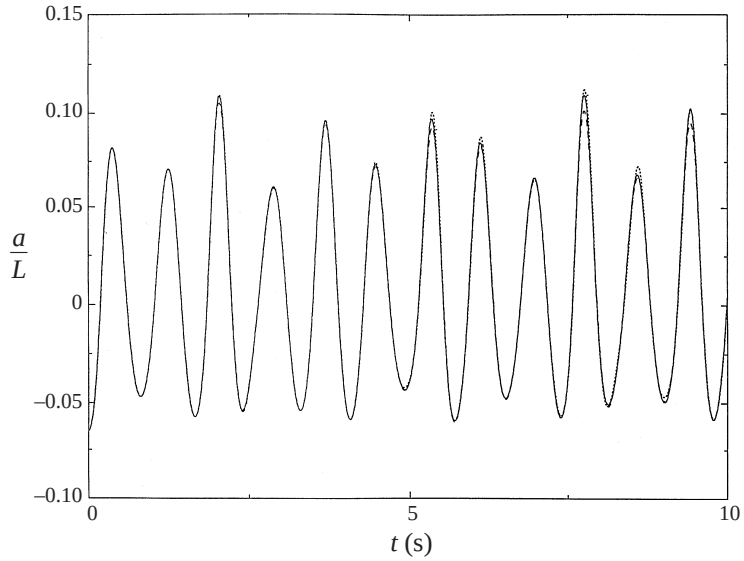

FIGURE 4. Evolution of the amplitude of a standing gravity–capillary wave computed to test the accuracy of the numerical methods. The solid line represents the nearly grid-size-independent boundary-integral solution. The dashed and dotted lines represent results of the vortex formulation obtained with 100 and 150 marker points, respectively.

Thus, in terms of efficiency, the vortex-sheet method outperforms the boundary-integral method.

Next, we compare the performance of the numerical methods for a large-amplitude motion. In figure 4, we present the time history of the amplitude of a standing gravity–capillary wave subject to a disturbance with initial amplitude $a_0/L = 0.065$ over twelve periods of oscillation. The physical conditions are $\rho_+ = 0$, $\rho_- = 1000\,\mathrm{kg\,m^{-3}}$, $L = 1.0\,\mathrm{m}$, $\tau = 0.072\,\mathrm{N\,m^{-1}}$, $g = 9.81\,\mathrm{m\ s^{-2}}$, and $\zeta = 0$. The boundary-integral solution was obtained using approximately 100 interfacial marker points – the actual number changed slightly in time due to regridding – and was confirmed to be accurate to within plotting resolution. The vortex-sheet solution was obtained with a fixed number of 100 or 150 points. The discrepancies between the three numerical solutions are most prominent at the peaks of the oscillations at long times. These comparisons suggest that when the amplitude of the interface is large compared to the wavelength of the perturbation, the boundary-integral method outperforms the vortex-sheet method for the same number of marker points.

4. Results and discussion

We begin presenting the results of dynamical simulations by considering the dynamics of a free surface corresponding to Atwood ratio $A = 1$, and then proceed to examine the effect of the density of the upper fluid. In all cases, the interface is perturbed by a sinusoidal wave of amplitude a_0 and wavelength L, while the distribution of the potential and strength of the vortex sheet retain their unperturbed zero values. Due to the large available parametric space, we only present results for typical case studies that illustrate the salient features of the motion. Additional case studies are presented by Wright (1999).

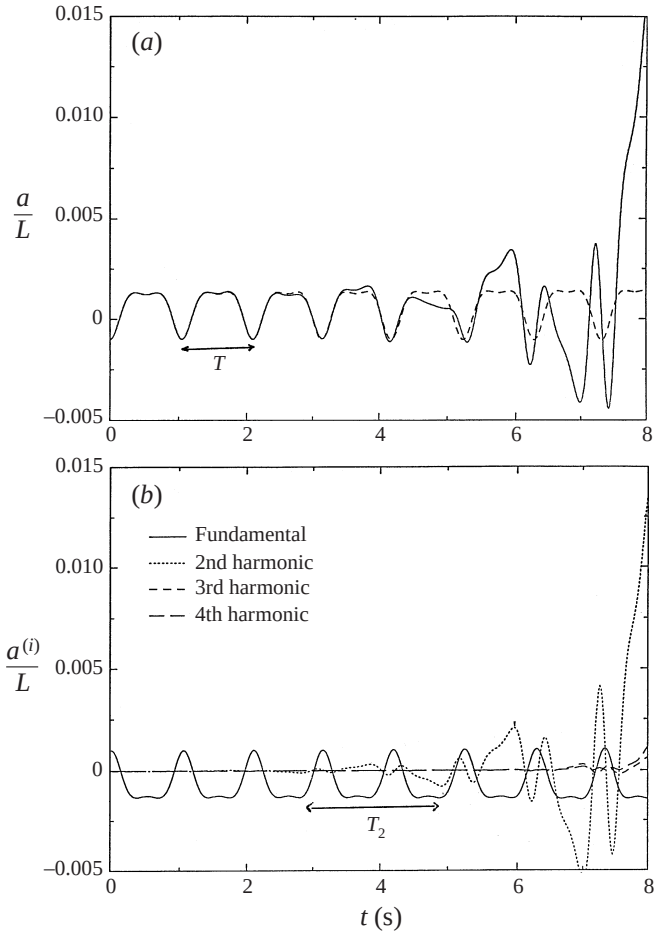

FIGURE 5. (*a*) Evolution of the amplitude of the interface for $p = 6.828$, $q = 4$, and $\delta = 0$, corresponding to the point labelled 'sb1' (stability boundary) in figure 2; the solid line represents the numerical solution, and the dashed line represents the solution of the Mathieu equation. (*b*) Evolution of the first four spatial harmonics. The second harmonic corresponds to the point labelled 'sb2' in figure 2, and its period is indicated by the arrow labelled 'T_2'.

4.1. *Deviation from the linear solution*

When the initial amplitude of the interface is small and the pair (p, q) lies on one of the stability boundaries in the Mathieu stability diagram, linear analysis predicts that the interface oscillates periodically while maintaining its initial amplitude. In figure 5(*a*), we present the time history of the amplitude of a small-amplitude disturbance with $a_0/L = 0.001$, for $p = 6.828$, $q = 4$, and $\delta = 0$, corresponding to the point labelled 'sb1' (stability boundary) in figure 2. These values of p and q correspond to the physical conditions: $\rho_+ = 0$, $\rho_- = 1000\,\mathrm{kg\,m^{-3}}$, $L = 1\,\mathrm{m}$, $g = 9.81\,\mathrm{m\,s^{-2}}$, $f = 11.494\,\mathrm{m\,s^{-2}}$, $\omega = 6.0092\,\mathrm{s^{-1}}$, $\tau = 0.072\,\mathrm{N\,m^{-1}}$, and $\zeta = 0$. Examination of figure 5(*a*) reveals that the boundary-integral solution closely follows the solution of the Mathieu equation up to 4 s. During this initial stage, the period of oscillation of the interface is nearly equal to that of the imposed forcing, $T = 0.956\,\mathrm{s}$, as predicted by the Floquet stability analysis. Significant deviations, however, occur at longer times. We note, in particular, that the numerical solution exhibits alternatingly

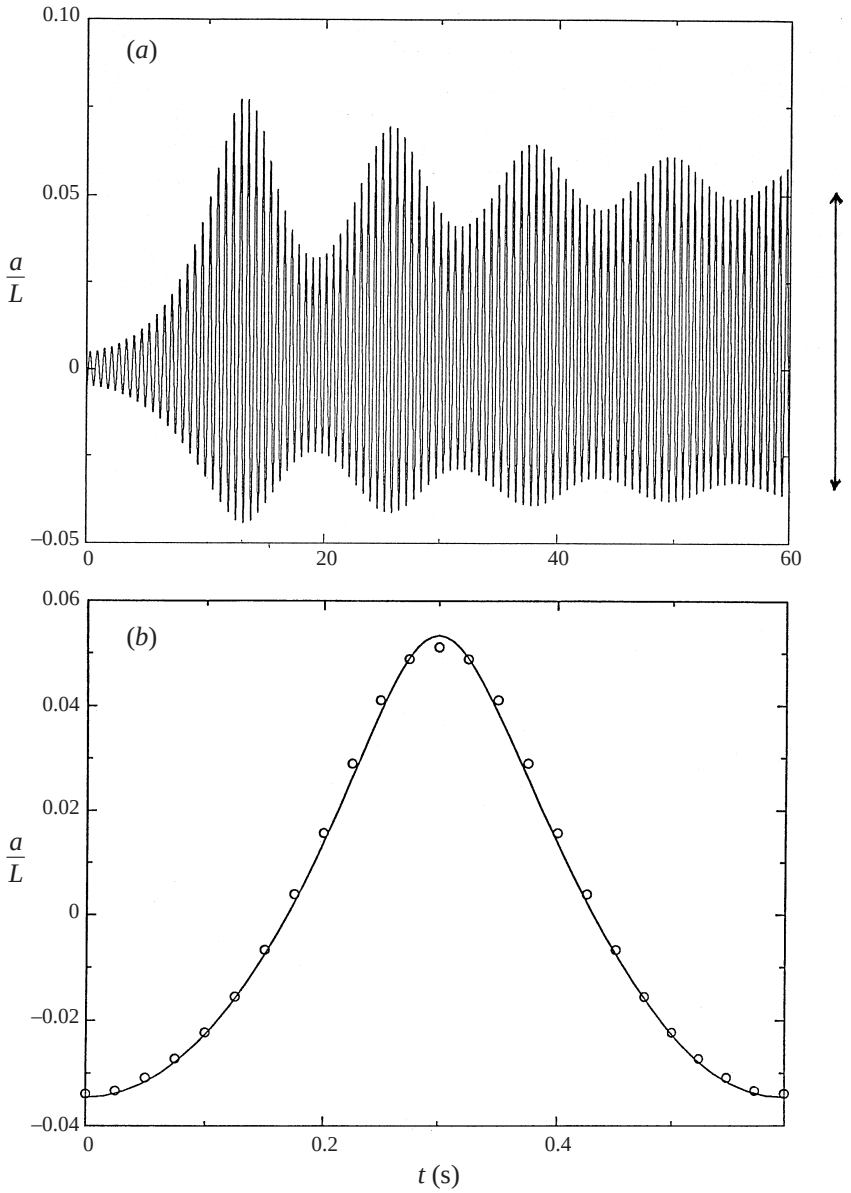

FIGURE 6 (*a*, *b*). For caption see facing page.

positive and negative displacements from the linearized prediction, and this suggests that the deviation is due to the growth of a temporal subharmonic wave due to nonlinear interactions.

In figure 5(*b*), we present the time histories of the first four spatial Fourier modes of the interfacial position, denoted as $a^{(i)}$, where i is an integer. The fundamental mode $a^{(0)}$ closely follows the linearized prediction over the entire length of the simulation, exhibiting a periodic behaviour, whereas the second-harmonic mode $a^{(1)}$ grows rapidly to dominate during the latter part of the simulation. The angular frequency of the second spatial mode is equal to half the angular frequency of

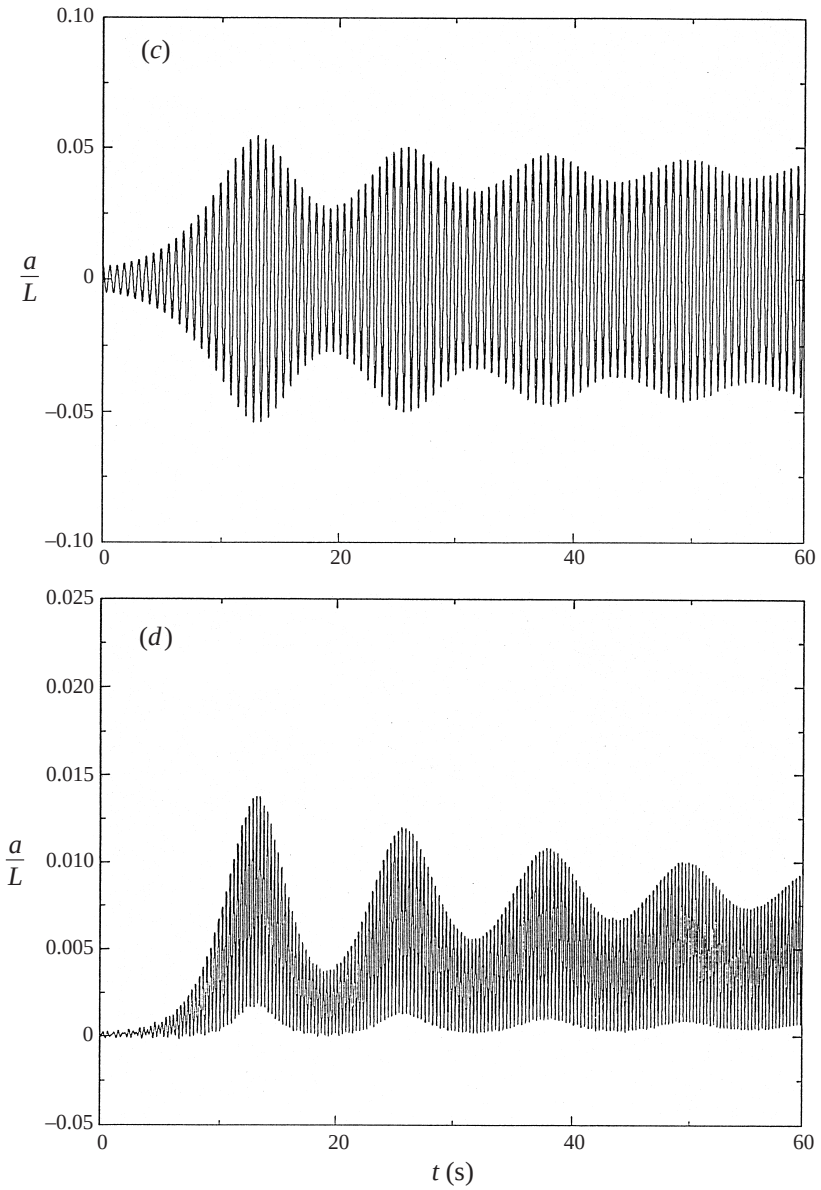

FIGURE 6. (*a*) Evolution of the amplitude of the interface for $p = 1$, $q = 0.055$, $\zeta = 0.7$ and $a_0/L = 0.005$. In the absence of damping, these conditions are represented by the point labelled 'd' in figure 2. The asymptotic wave height obtained by Jiang *et al.* (1996) is indicated by the vertical arrow on the right side of the figure. (*b*) Asymptotic wave shape at maximum amplitude. The solid line represents the results obtained with the boundary integral method, and the symbols represent the numerical results of Jiang *et al.* (1996). (*c*, *d*) Evolution of the fundamental and second spatial harmonics.

the fundamental mode, and this suggests that the instability is subharmonic relative to the fundamental mode. This behaviour, however, is not surprising: The pair (p, q) corresponding to the second-harmonic mode is located at the point labelled 'sb2' in figure 2, which lies within the unstable regime of the Mathieu stability diagram. The imaginary part of the Floquet exponent for the second-harmonic

mode obtained by setting the determinant of (2.10) with $p = 13.66$, $q = 8.0$, and $\delta = 0$, is found to be $\sigma_i = 0.318$. Accordingly, the Floquet analysis predicts that the maximum amplitude of the second-harmonic mode grows exponentially as $\exp(0.159\ \omega t)$ which is in excellent agreement with the results of the numerical simulations. The numerical results shown in figure 5(*b*) suggest that higher harmonics become significant at longer times, also contributing to the fully nonlinear motion.

4.2. *Comparison with the experiments of Jiang et al.*

When the amplitude of the interface is small, and the pair (p, q) lies within one of the unstable regions of the Mathieu stability diagram, linear analysis predicts that the interface oscillates with a maximum amplitude that grows exponentially in time. In figure 6, we present numerical solutions generated by the boundary integral method for $p = 1.0$, $q = 0.055$, and $\delta = 0.0069$, corresponding to the physical conditions: $\rho_+ = 0$, $\rho_- = 1000\,\mathrm{kg\,m^{-3}}$, $L = 0.6\,\mathrm{m}$, $\tau = 0.072\,\mathrm{N\,m^{-1}}$, $g = 9.81\,\mathrm{m\,s^{-2}}$, $f = 1.0915\,\mathrm{m\,s^{-2}}$, $\omega = 20.295\,\mathrm{s^{-1}}$, and $\zeta = 0.07\,\mathrm{s^{-1}}$. In the absence of damping, the pair (p, q) is represented by the point labelled 'd' (damped) in figure 2. These physical conditions correspond to the experiments and accompanying simulations for an air–water interface by Jiang *et al.* (1996). It should be noted that the magnitude of the damping coefficient ζ, selected to reconcile experiments and simulation, is two orders of magnitude larger than the theoretical value for dissipation within the bulk of a viscous fluid undergoing small oscillations, as given by Landau & Lifshitz (1987). This large difference emphasizes the phenomenological nature of ζ and the significance of viscous dissipation within the oscillatory boundary layers, along the container walls, and over the free surface, as discussed by Henderson & Miles (1994) and Henderson (1998).

The evolution of the maximum amplitude of the interface shown in figure 6(*a*) is consistent with the numerical and experimental results of Jiang *et al.* (1996). After an initial period characterized by rapid growth, the maximum amplitude of the interface decays in an oscillatory fashion, and a periodic standing wave is established. The asymptotic wave height obtained by Jiang *et al.* (1996), indicated by the vertical arrow on the right, is in good agreement with that predicted by our simulations. In figure 6(*b*), we plot, with the solid line, the shape of the standing wave at the peak of the oscillation, and compare it with the measurements of Jiang *et al.* (1996) represented by the circles, to find good agreement. The sharpness of the wave crest relative to the trough is due to contributions from higher spatial harmonics. To illustrate this feature explicitly, in figure 6(*c*, *d*), we present the time histories of the first and second spatial Fourier modes of the evolving interface. At long times, the fundamental mode oscillates harmonically at a constant amplitude, while the second mode makes a positive contribution that is responsible for the peaked configuration at maximum amplitude. The contributions of the third and higher harmonics are negligible in this case.

4.3. *Transition to a fully nonlinear motion*

As the amplitude of the imposed acceleration is raised, a fully nonlinear motion is established at long times, even from small-amplitude perturbations. Consider a perturbation with $a_0/L = 0.001$, imposed on a physical system with $\rho_+ = 0$, $\rho_- = 1000\,\mathrm{kg\,m^{-3}}$, $L = 1.0\,\mathrm{m}$, $\tau = 0.072\,\mathrm{N\,m^{-1}}$, $g = 9.81\,\mathrm{m\,s^{-2}}$, $f = 4.905\,\mathrm{m\,s^{-2}}$,

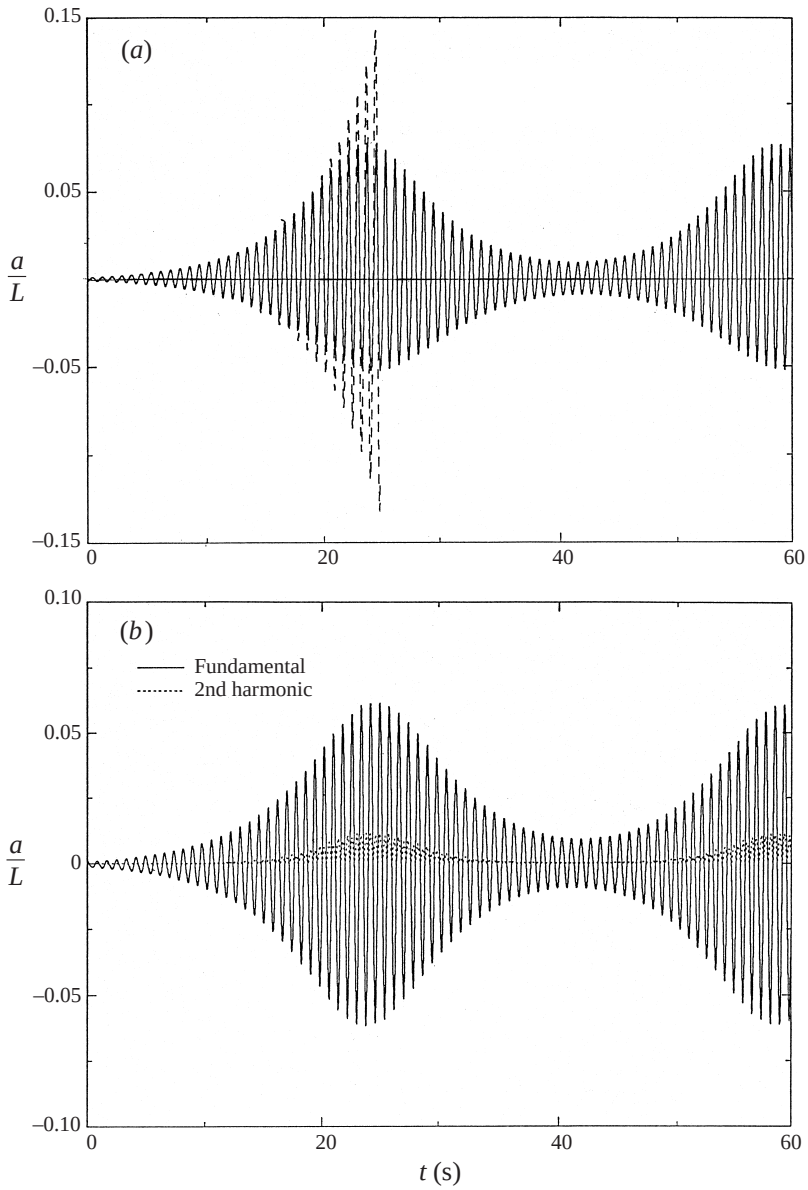

FIGURE 7. (*a*) Evolution of the amplitude of the interface for $p = 4$, $q = 1$, corresponding to the point labelled 'e1' in figure 2. The solid line represents the boundary-integral solution, and the dashed line represents the solution of Mathieu equation's equation. (*b*) Evolution of the fundamental and second harmonic spatial modes.

$\omega = 7.851\,\mathrm{s}^{-1}$, and $\zeta = 0\,\mathrm{s}^{-1}$, corresponding to $p = 4.0$, $q = 1.0$, and $\delta = 0$. This pair of (p, q) is represented by the point labelled 'el'(exponenetial) in figure 2; the associated imaginary part of the Floquet exponent has the positive value $\sigma_i = 0.046$, predicting exponential growth. In figure 7(*a*), we display the time history of the amplitude of the free surface over seventy-five oscillations of the interface computed by the boundary-integral method, represented by the solid line, along with the linear predictions computed by solving Mathieu equation, represented by the

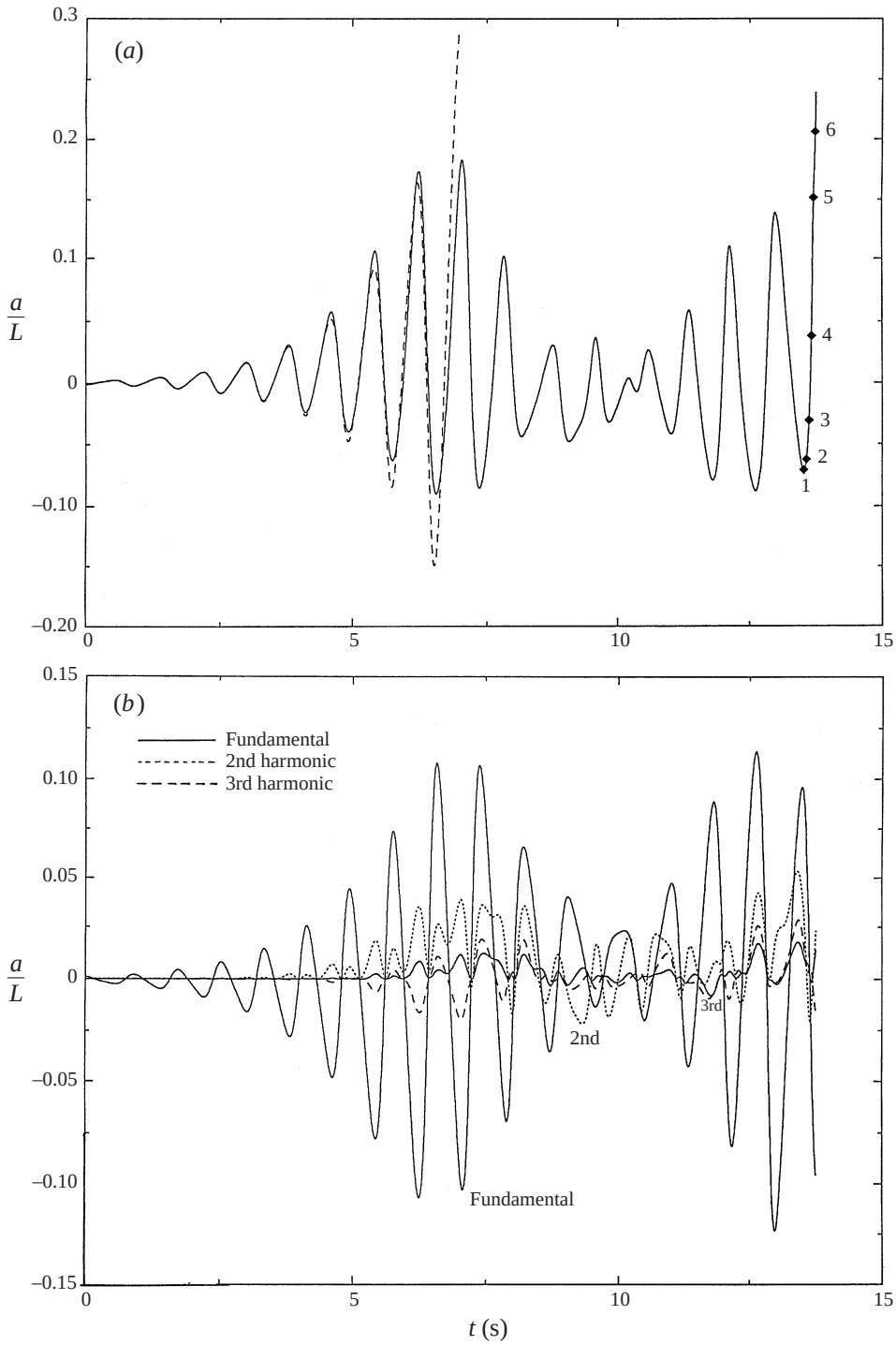

FIGURE 8 (*a*, *b*). For caption see facing page.

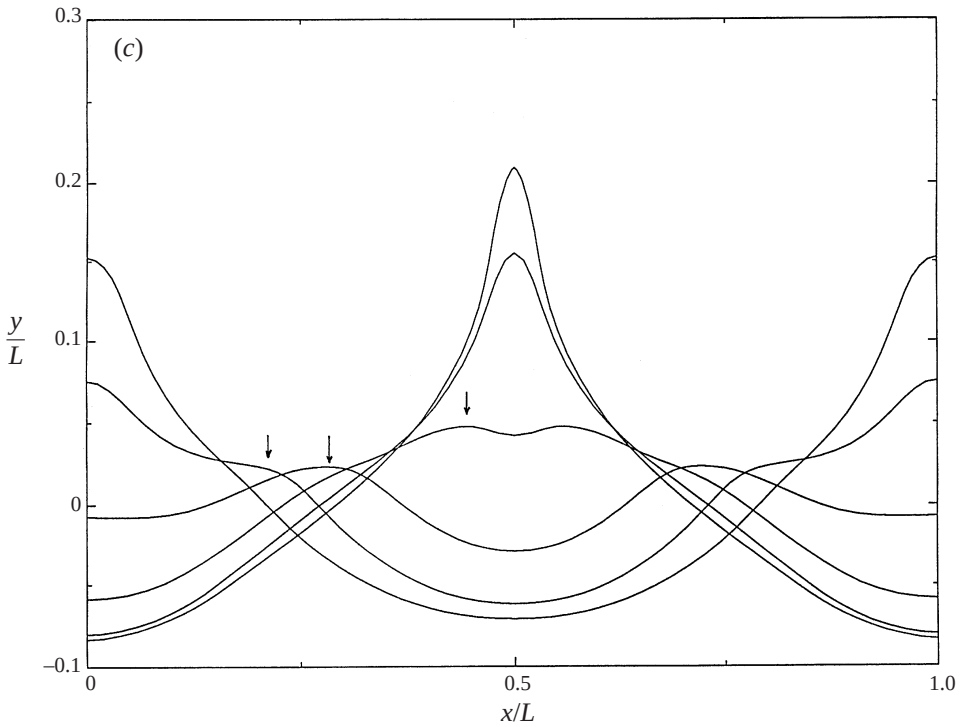

FIGURE 8. (*a*) Evolution of the amplitude of the interface obtained for $p = 4$, $q = 2$, corresponding to the point labelled 'e2' in figure 2. The solid line represents the boundary integral solution, and the dashed line represents the solution of Mathieu's equation. (*b*) Time histories of the first to fourth harmonic modes (*c*) Interfacial shapes corresponding to the points labelled 1–6 in (*a*). The arrows indicate the crest of a symmetric harmonic disturbance moving toward the centre.

dashed line. During the initial period of rapid growth, the linearized prediction closely approximates the numerical solution, but important deviations arise when the maximum amplitude of the interface has become approximately twenty times the initial value. This point corresponds to the time when the higher harmonics of the spatial interface Fourier expansion become significant, as shown in figure 7(*b*). For $t > 20$ s, the interfacial oscillation develops a slow modulation around a mean value that is similar to that observed in the damped solution shown earlier in figure 6(*a*). This behaviour suggests that the occurrence of the slow time scale is not due to viscous damping, but it is an intrinsic feature of the nonlinear motion.

Doubling the magnitude of the acceleration, while leaving the remaining physical parameters unchanged, yields the dimensionless parameters $p = 4.0$, $q = 2.0$ and $\delta = 0$ represented by the point labelled 'e2' in figure 2. The associated imaginary part of the Floquet exponent is found to be $\sigma_i = 0.7146$, predicting rapid growth. Figure 8(*a*) displays the evolution of the amplitude of the interface, computed with the boundary-integral method, along with the linearized predictions. The numerical solution reveals that, after an initial period of rapid growth, the maximum amplitude of the interface decays and then shows a rather irregular behaviour. This long-time motion contrasts with that shown in figures 6(*a*) and 7(*a*). In figure 8(*b*), we present the evolution of the first four harmonic spatial modes. For $t < 5$ s, the magnitude of the higher harmonics is comparable to that

for the lightly forced case shown in figure 7(*b*). As time progresses, however, the amplitude of the second harmonic changes sign and higher harmonics become significant.

The significant appearance of higher harmonics in the case of strong forcing is associated with the formation of paired waves travelling within each period. The constructive interference of these waves yields momentary geometrical peaks with high curvature. In figure 8(*c*), we display the shape of the interface at a sequence of times between $t = 13.5\,\mathrm{s}$ and $t = 13.7\,\mathrm{s}$. A pair of travelling waves, indicated by arrows, moves symmetrically toward the centre of the figure and combine to yield a sharp peak. When the curvature of the interface has become large, sudden local acceleration occurs due to the effects of surface tension. This behaviour is consistent with results reported recently by Schultz *et al.* (1998), who found that the presence of surface tension prevents the formation of cusped waves. In the absence of adaptive time stepping, the large local velocity is responsible for numerical instabilities that result in the formation of physically irrelevant structures. In the present simulation, the interface intersected itself shortly after the formation of the peak shown in figure 8(*c*).

4.4. *Effect of the Atwood ratio*

We proceed next to investigate the effect of the Atwood ratio A under conditions where the acceleration of gravity is negligible compared to the amplitude of the imposed harmonic acceleration, and the ratio f/g is large. Unless stated otherwise, all simulations correspond to a perturbation with initial amplitude $a_0/L = 0.01$, and physical conditions $\rho_- = 1000\,\mathrm{kg\,m^{-3}}$, $L = 1.0\,\mathrm{m}$, $\tau = 0.072\,\mathrm{N\,m^{-1}}$, $g = 0\,\mathrm{m\,s^{-2}}$, $f = 0.01\,\mathrm{m\,s^{-2}}$, $\omega = 0.26728\,\mathrm{s^{-1}}$, and $\zeta = 0\,\mathrm{s^{-1}}$. The density of the upper fluid ρ_+ is varied to produce a range of Atwood ratios. As A is raised from zero to unity, corresponding pairs (p, q) move from a stable regime near the origin of the Mathieu stability plane shown in figure 9, confined in the range $0 < A < 0.2$, into a regime where the first subharmonic mode becomes unstable while the second- and third-harmonic modes remain stable. The pairs (p, q) corresponding to the first harmonic fall within a stable regime, as depicted by the line labelled 'second harmonic' in figure 9. Within this parametric framework, we obtain four distinct regimes of evolution with strikingly different behaviours, identified as *linearly stable*, *slow modulation*, *plume formation*, and *droplet ejection*.

Within the linearly stable regime $0 < A < 0.2$, prevailing between the points labelled 1 and 2 in figure 9, the densities of the upper and lower fluids are of the same order of magnitude, the interface retains a nearly sinusoidal shape during the oscillations, and the evolution of the amplitude of the fundamental wave matches closely that predicted by Mathieu's equation.

Within the slow modulation regime, the shape of the interface remains smooth at all times, but it no longer has a sinusoidal shape. The fluid responds to the imposed acceleration on a time scale that is fast compared to the period of the acceleration, and there is ample time for the interface to relax before the next cycle begins. In this manner, the deformations suffered during successive cycles do not build up into a violent motion. Examples of slow modulation occurring for $0.22 < A < 0.5$, are presented in figure 10, showing the evolution of the amplitude of the interface and of the fundamental and second spatial harmonic modes for four values of A. The angular frequency of the modulated temporal oscillations is equal to half the angular frequency of the imposed forcing, in agreement with

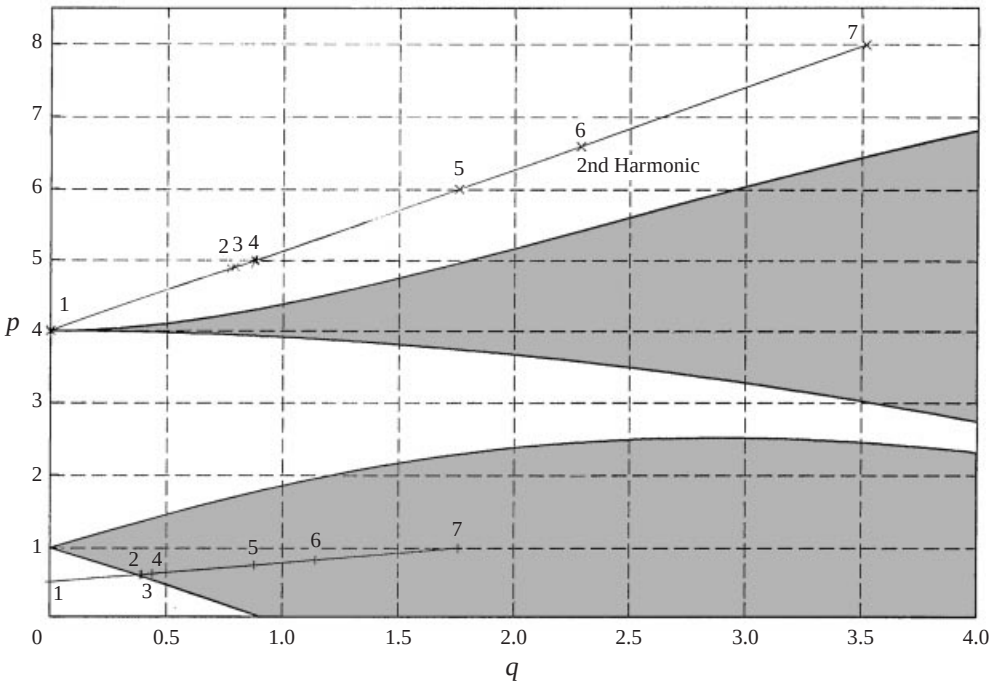

FIGURE 9. Location of the parametric studies with respect to the Atwood ratio on the Mathieu stability graph.

the predictions of the Floquet stability analysis. In all cases, we observe an initial exponential growth at a rate that is consistent with the growth rate predicted by the Floquet analysis. Slow modulation of the amplitude of the interface then follows corresponding to a cyclic variation in the amplitude of the second harmonic waves. The behaviour in this regime is qualitatively similar to that for $A = 1$, $p = 4$, $q = 1$ discussed in §4.2. The absence of damping confirms once again that the slow modulation of the maximum amplitude is an intrinsic feature of the nonlinear motion.

The sequence 10(*a–d*) illustrates that as the value of the Atwood is raised from 0.22 to 0.5, the second spatial harmonic wave becomes increasingly important. The period of oscillation of this wave is in good agreement with that predicted by linear theory for monochromatic waves. Once excited, the second harmonic continues to oscillate as though it evolved in isolation, in spite of its significant amplitude. For example, in figure 10(*b*) we observe that when the peak amplitude of the fundamental wave passes through a minumum within the time interval $500\,\mathrm{s} < t < 600\,\mathrm{s}$, the evolution of the amplitude of the second-harmonic mode remains effectively unchanged. In computer animation, one sees several cycles of this harmonic oscillation before the subsequent growth of the fundamental.

As the Atwood number is raised further, Floquet theory predicts faster growth of the fundamental mode, and consequent faster appearance and growth of the second harmonic. In the plume formation regime $0.5 < A < 0.7$, the interface suffers local instabilities that cause plume-like structures to develop in a spontaneous fashion. Figure 11(*a*) displays the evolution of the amplitude of the interface in comparison with the imposed forcing. At short times, the former shows a dis-

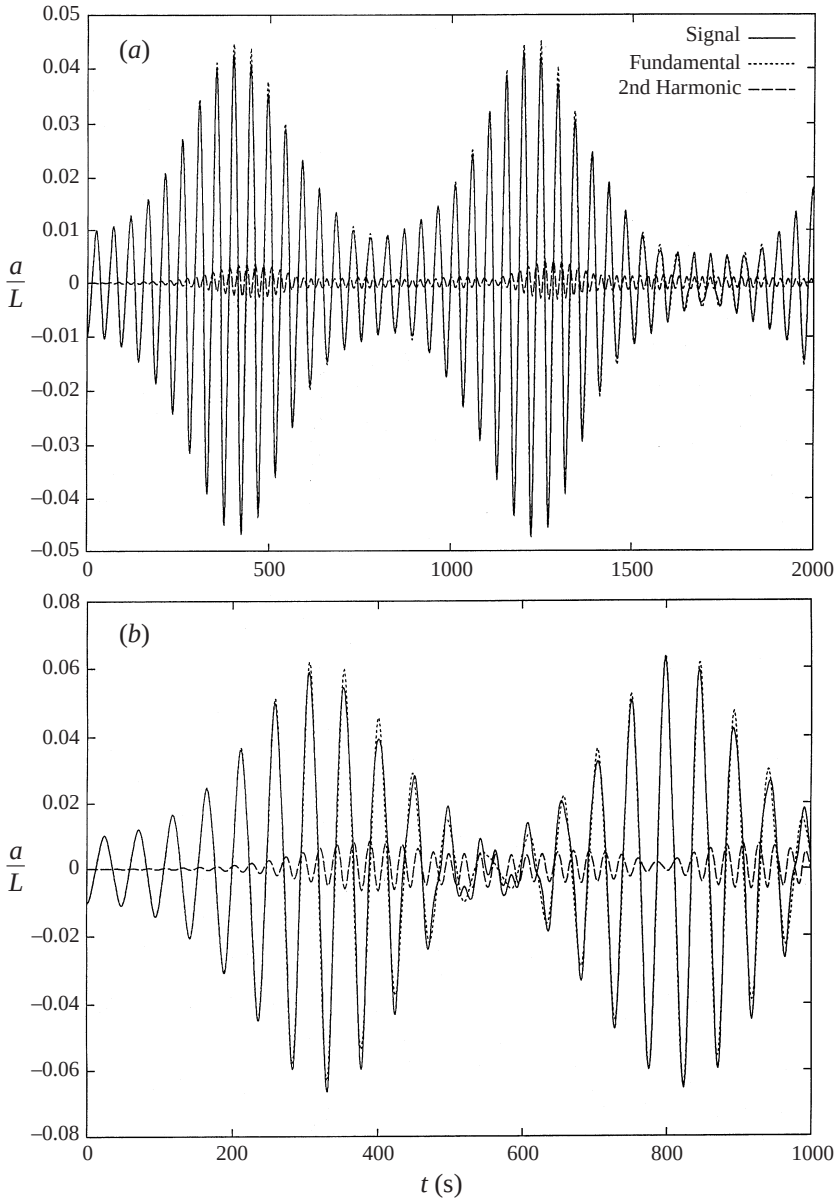

FIGURE 10 (*a*, *b*). For caption see facing page.

torted oscillation whose period is equal to twice that of the imposed acceleration. At long times, the height of the interface reaches a minimum at about $t = 46\,\mathrm{s}$, whereupon the external acceleration completes its second cycle, and then fluctuates during the next two cycles. During the second and third cycle, a Kelvin–Helmholtz instability develops along the vertical portions of the vortex sheet causing the interface to roll up into a plume-like configuration, as shown in figure 11(*b*). It is well established that a singularity in curvature, manifested as a kink or corner, precedes the roll up of the vortex sheet in the absence or presence of surface tension (e.g. Hou, Lowengrub & Shelley 1997; Cowley, Baker & Tanveer 1999), but

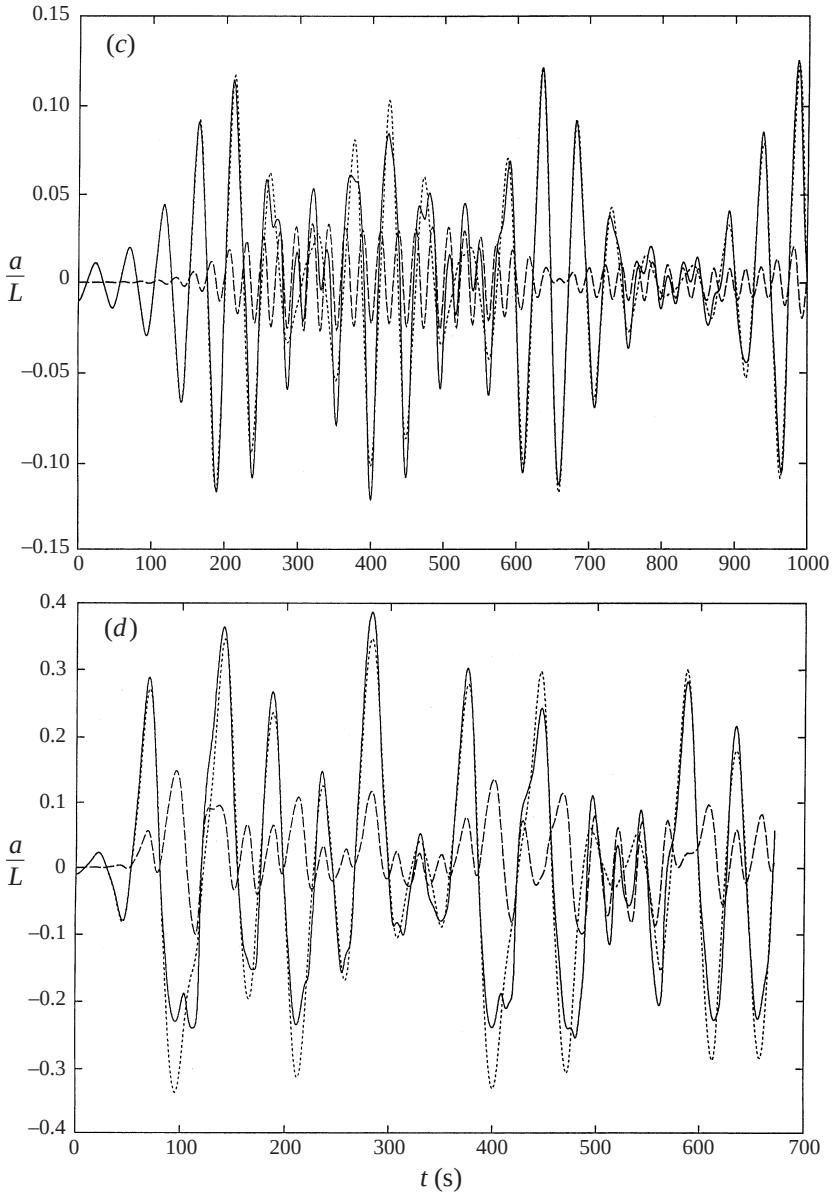

FIGURE 10. Evolution of the amplitude of the interface and spatial harmonics for the conditions described in the text, for Atwood ratio (*a*) $A = 0.22$, (*b*) $A = 0.225$, (*c*) $A = 0.25$, and (*d*) $A = 0.50$. As the Atwood ratio is increased, the amplitude of the oscillation becomes increasingly larger eventually leading to droplet ejection.

our numerical method is not sufficiently accurate to probe the fine features of the motion.

In the droplet ejection regime, $0.7 < A < 1.0$, we observe the formation and ejection of two-dimensional droplets from the points of highest elevation. Numerical experimentation showed that the process of droplet formation is insensitive to the initial amplitude of the perturbation. Figure 12(*a*) shows the evolution of the maximum amplitude of the interface for $A = 1.0$, and figure 12(*b*, *c*) shows snapshots of the evolving interface during the process of drop formation; the corresponding

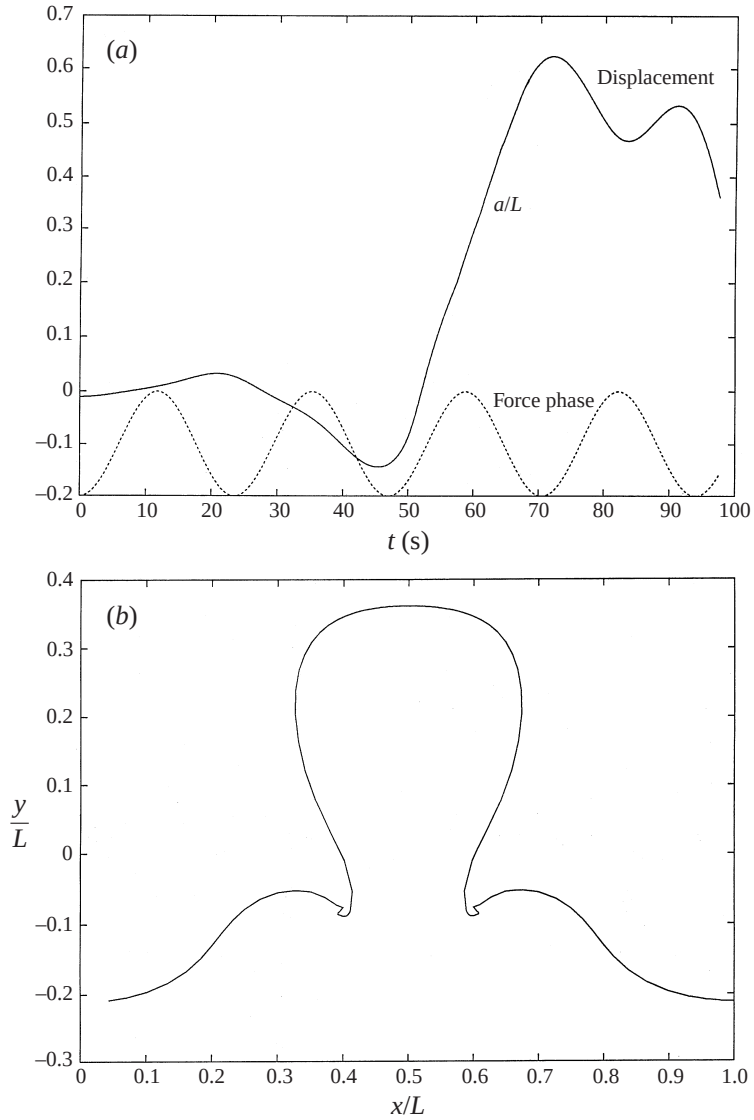

FIGURE 11. (*a*) Evolution of the amplitude of the interface for $A = 0.65$, plotted along with the phase of the external acceleration. This figure clearly shows the subharmonic nature of the interfacial waves. (*b*) Shape of the interface at end of the simulation showing the formation of a plume.

times are indicated by the symbols in figure 12(*a*). Physically, the displacement of the interface from the unperturbed position accumulates during successive cycles, rather than relaxing as was observed for smaller values of A. A certain mass of lower fluid is entrained into the upper fluid in the form of a jet, and a droplet develops which is then pinched off during the next cycle of the oscillation. If the motion were axisymmetric or three-dimensional, the thread would break up due to capillarity into a series of satellite drops. The attachment point of the thread connecting the drop to the lower fluid is the site of a corner that causes the numerical computation to fail at a certain time. Figure 12(*d*) depicts the evolution of

the strength of the interfacial vortex sheet. As time progresses, the strength amplifies near the base of the drops, possibly leading to singular behaviour at long times.

Jiang *et al.* (1998) reported laboratory observations of the dynamics of Faraday ways under conditions corresponding to the lowest unstable regime shown in figure 9, properly shifted to account for the effects of viscous dissipation. Their results revealed that, as the forcing amplitude is raised, whereupon the pair (p, q) moves further away from the apex of the stability boundary, the standing waves undergo an intriguing transformation similar to that reported in this subsection with respect to the Atwood ratio. Jiang *et al.* (1998) found that, as the forcing amplitude is raised, small plunging breakers first appear on either side of a dimpled crest, and then period tripling occurs with breaking developing in every two out of three temporal periods. The period-tripled evolution involves a wave profile with a sharp crest followed by violent breaking and drop formation; a profile with dimpled or flat crest and a double plunger on either side; and a profile with a round crest.

Profiles qualitatively similar to those corresponding to the three modes of the period-tripled dynamics were observed in our simulations, although numerical difficulties prevented an exact reproduction; the numerical simulations break down when a sharp wave breaks up to eject a drop. It is reassuring, however, that period tripling is clearly manifested in the numerical results for conditions close to those identified by Jiang *et al.* (1998). In figure 13(*a*), we present the evolution of the maximum elevation of an air–water interface for $\rho_- = 1000\,\mathrm{kg\,m^{-3}}$, $\rho_+ = 1\,\mathrm{kg\,m^{-3}}$, $L = 0.6\,\mathrm{m}$, $\tau = 0.072\,\mathrm{N\,m^{-1}}$, $g = 9.81\,\mathrm{m\,s^{-2}}$, $f = 1.78\,\mathrm{m\,s^{-2}}$, $\omega = 19.395\,\mathrm{s^{-1}}$, and $\zeta = 0\,\mathrm{s^{-1}}$, corresponding to $p = 1.09$ and $q = 0.10$. At long times, a nearly periodic pattern that is repeated at every third cycle is established. The general features of this graph are similar to those presented in figure 16(*a*) of Jiang *et al.* (1998) for a period-tripled breaker. Wright (1999) discusses pseudo-phase-space portraits that are similar to those presented by Jiang *et al.* (1998). The interfacial profiles corresponding to the three successive peaks indicated by the arrows in figure 13(*a*), shown in figure 13(*b*), are precursors of the three modes identified by Jiang *et al.* (1998). This comparison strongly suggests that period tripling is not due to viscous effects, neither it is associated with the dynamics of the contact line, but develops as the result of a nonlinear motion in the context of irrotational flow.

5. Concluding remarks

One of the most significant findings of the present numerical investigation is the development of plumes at moderate values of the Atwood ratio, and the formation and ejection of droplets at the extremes of the interfacial waves at higher values of the Atwood ratio. The early stages of droplet ejection are qualitatively similar to those of plume formation, but differences arise during the late stages when the vertical stem of the plume narrows to a thin filament connecting the droplet with the bulk of the lower fluid rather than developing a secondary instability. This behaviour is similar to that identified in previous numerical studies of the Rayleigh–Taylor instability (e.g. Ceniceros & Hou 1998). Our results are in agreement with the experimental observations of Goodrich, Shi & Lathrop (1996) and Jiang *et al.* (1998) who observed the ejection of nearly axi-

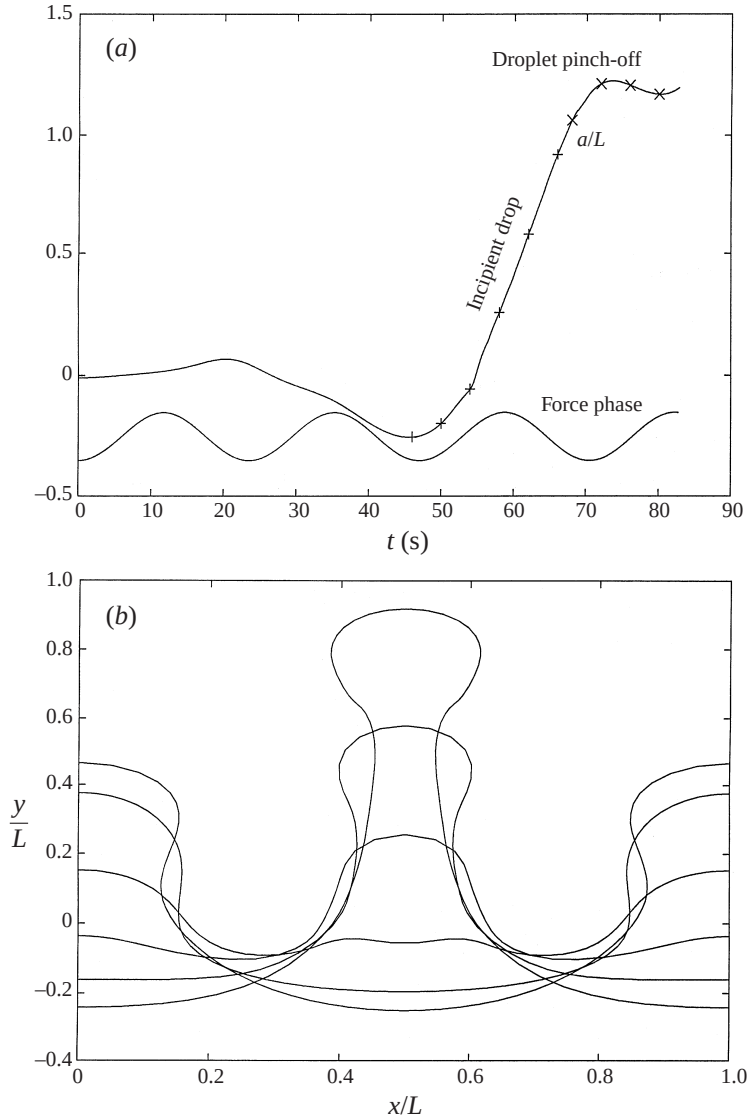

FIGURE 12 (*a*, *b*). For caption see facing page.

symmetric droplets from a vibrating air–water interface, marking the onset of mixing.

Our formulation accounted for the effects of viscosity by means of a phenomenological coefficient whose physical relevance has been established only for small-amplitude oscillations. In the case of a free surface, but not an interface, weak viscous effects at high Reynolds numbers may be accounted for by means of a boundary-layer analysis, but implementation difficulties associated with the seaming of the boundary layers at free-surface stagnation points are a serious impediment. Direct numerical simulation on the basis of the Navier–Stokes equations is the only viable alternative for studying large-amplitude motions. The development of numerical methods for two-dimensional flow based on domain mapping followed by spectral expansions is the subject of ongoing investigation.

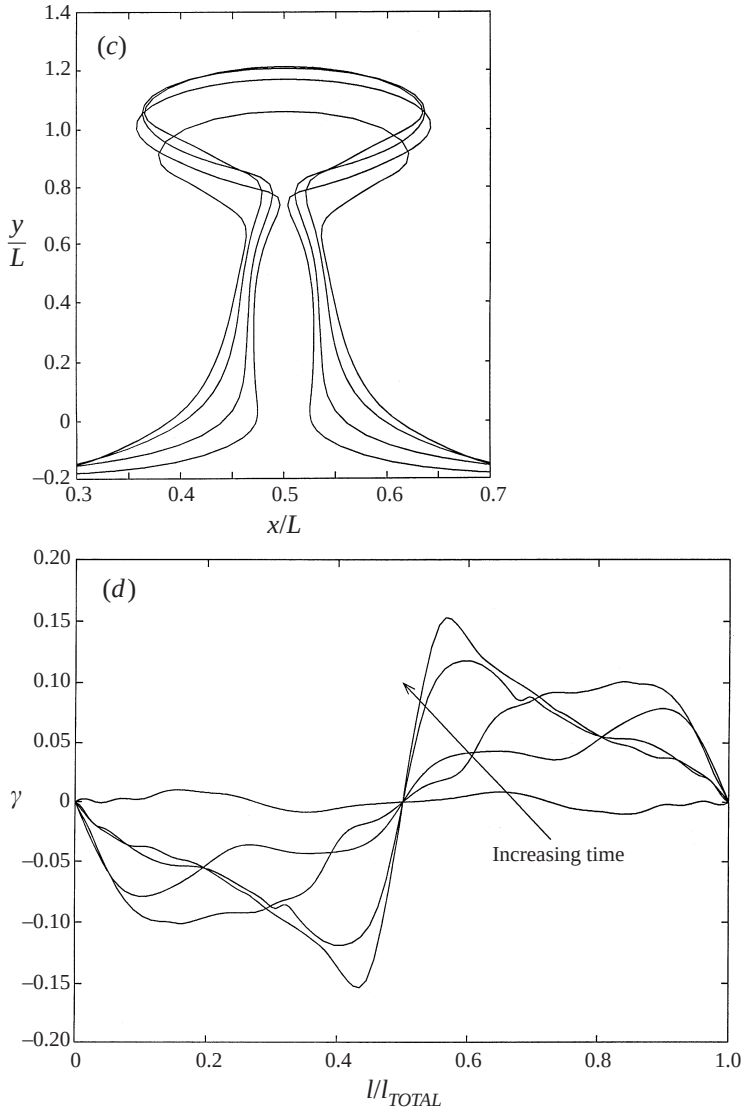

FIGURE 12. (*a*) Evolution of the amplitude of the interface for $A = 1.0$, plotted along with the phase of the external acceleration. The symbols in this graph correspond to the times of the snapshots displayed in (*b*, *c*) showing the formation and pinch-off of a droplet. (*d*) Evolution of the strength of the interfacial vortex sheet, plotted against normalized arclength l, corresponding to the snapshots of incipient drop formation shown in (*b*).

To study the nonlinear dynamics of doubly-periodic patterns along a free surface or interface between two inviscid fluids, it is necessary to extend the boundary-integral and vortex methods described in this paper to three dimensions. Pozrikidis (1999*b*) recently developed a boundary-element method for simulating the self-induced motion of closed or periodic three-dimensional vortex sheets, based on evolution laws for the strength of the vortex sheet or for the density of the effective dipole or circulation along the vortex sheet. The use of the doubly-periodic Green's function of Laplace's equation, and its efficient computation in terms of Ewald sums

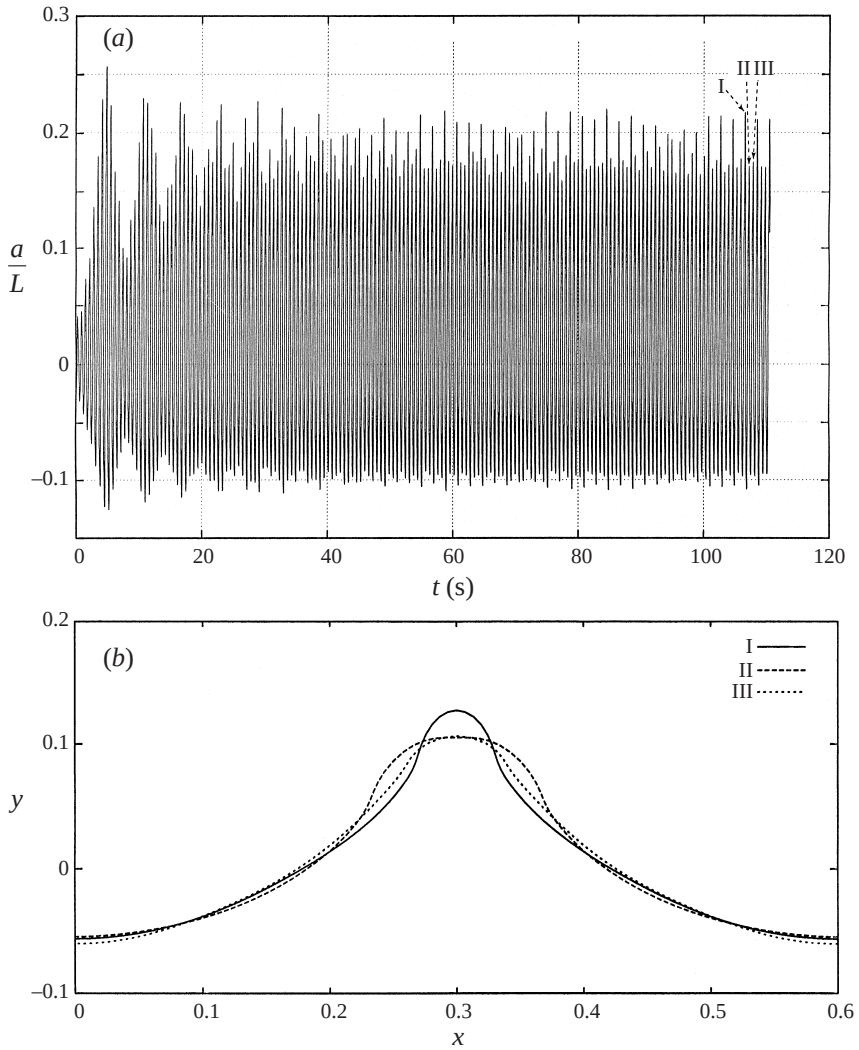

FIGURE 13. (*a*) Evolution of the amplitude of the interface for $p = 1.091$ and $q = 0.10$, showing the occurrence of period-tripled waves. (*b*) Interface profiles corresponding to the three successive peaks indicated by arrows in (*a*).

are two crucial components of the numerical method. The adaptation of this general methodology to the problem of Faraday oscillations is the subject of ongoing research.

This research has been supported by NASA.

REFERENCES

ABRAMOWITZ, M. & STEGUN, I. A. 1964 *Handbook of Mathematical Functions*. Dover.

BAKER, G. R., CAFLISCH, R. E. & SIEGEL, M. 1993 Singularity formation during Rayleigh–Taylor instability. *J. Fluid Mech.* **252**, 51–78.

BAKER, G. R., MEIRON, D. I. & ORSZAG, S. A. 1982 Generalized vortex methods for free-surface flow problems. *J. Fluid Mech.* **123**, 477–501.

Benjamin, T. N. & Ursell, F. 1954 The stability of the plane free surface of a liquid in vertical periodic motion. *Proc. R. Soc. Lond.* A **225**, 505–515.

Ceniceros, H. D. & Hou, T. Y. 1998 Convergence of a non-stiff boundary integral method for interfacial flows with surface tension. *Math. Comput.* **221**, 137–182.

Cerda, E. A. & Tirapegui, E. L. 1998 Faraday's instability in viscous fluid. *J. Fluid Mech.* **368**, 195–228.

Coddington, E. A. & Levinson, N. 1955 *Theory of Ordinary Differential Equations.* McGraw-Hill.

Cowley, S. J., Baker, G. R. & Tanveer, S. 1999 On the formation of Moore curvature singularities in vortex sheets. *J. Fluid Mech.* **378**, 233–267.

Craik, A. D. D. & Armitage, J. 1995 Faraday excitation, hysteresis and wave instability in a narrow rectangular wave tank. *Fluid Dyn. Res.* **15**, 129–143.

Crawford, J. D., Gollub, J. P. & Lane, D. 1993 Hidden symmetries of parametrically forced waves. *Nonlinearity* **6**, 119–164.

Douady, S. 1990 Experimental study of the Faraday instability. *J. Fluid Mech.* **221**, 383–409.

Edwards, W. S. & Fauve, S. 1993 Parametrically excited quasicrystalline surface waves. *Phys. Rev.* E **47**, R788–791.

Edwards, W. S. & Fauve, S. 1994 Patterns and quasi-patterns in the Faraday experiment. *J. Fluid Mech.* **278**, 123–148.

Fauve, S., Kumar, L., Laroche, C., Beysens, D. & Garrabos, Y. 1992 Parametric instability of a liquid-vapour interface close to the critical point. *Phys. Rev. Lett.* **68**, 3160–3163.

Goodrich, C. L., Shi, W. T., Hentschel, H. G. E. & Lathrop, D. P. 1997 Viscous effects in droplet-ejecting capillary waves. *Phys. Rev.* E **56**, 472–475.

Goodrich, C. L., Shi, W. T. & Lathrop, D. P. 1996 Threshold dynamics of singular gravity–capillary waves. *Phys. Rev. Lett.* **76**, 1824–1827.

Henderson, D. M. 1998 Effects of surfactants on Faraday-wave dynamics. *J. Fluid Mech.* **365**, 89–107.

Henderson, D. M. & Miles, J. W. 1994 Surface-wave damping in a circular cylinder with a fixed contact line. *J. Fluid Mech.* **275**, 285–299.

Higdon, J. J. L. & Pozrikidis, C. 1985 The self-induced motion of vortex sheets. *J. Fluid Mech.* **150**, 203–234.

Hou, T. Y., Lowengrub, J. S. & Shelley, M. J. 1997 The long-time motion of vortex sheets with surface tension. *Phys. Fluids* **9**, 1933–1954.

Jiang, L., Ting, C. L., Perlin, M. & Schultz, W. W. 1996 Moderate and steep Faraday waves: instabilities, modulation and temporal asymmetries. *J. Fluid Mech.* **329**, 275–307.

Jiang, L., Ting, C. L., Perlin, M. & Schultz, W. W. 1998 Period tripling and energy dissipation of breaking standing waves. *J. Fluid Mech.* **369**, 273–299.

Jordan, D. W. & Smith, P. 1987 *Nonlinear Ordinary Differential Equations.* Oxford University Press.

Kudrolli, A. & Gollub, J. P. 1996*a* Patterns and spatiotemporal chaos in parametrically forced surface waves: A systematic survey at large aspect ratio. *Physica* D **97**, 133–154.

Kudrolli, A. & Gollub, J. P. 1996*b* Localized spatiotemporal chaos in surface waves. *Phys. Rev.* E **54**, R1052–1055.

Kumar, K. & Bajaj, K. M. S. 1995 Competing patterns in the Faraday experiment. *Phys. Rev.* E **52**, R4606–4609.

Kumar, K. & Tuckerman, L. S. 1994 Parametric instability of the interface between two fluids. *J. Fluid Mech.* **279**, 49–68.

Kwak, S. & Pozrikidis, C. 1998 Adaptive triangulation of evolving, closed or open surfaces by the advancing-front method. *J. Comput. Phys.* **145**, 61–88.

Landau, L. D. & Lifshitz, E. M. 1987 *Fluid Mechanics.* Pergamon.

Longuet-Higgins, M. S. & Cokelet, E. D. 1976 The deformation of steep surface waves on water. I. A numerical method of computation. *Proc. R. Soc. Lond.* A **350**, 1–26.

Mercer, G. N. & Roberts, A. J. 1992 Standing waves in deep water: Their stability and extreme form. *Phys. Fluids* A **4**, 259–269.

Mesquita, O. N., Kane, S. & Gollub, J. P. 1992 Transport by capillary waves: fluctuating Stokes drift. *Phys. Rev.* A **45**, 3700–3705.

Miles, J. 1984*a* Nonlinear Faraday resonance. *J. Fluid Mech.* **146**, 285–302.

Miles, J. 1984*b* Parametrically excited solitary waves. *J. Fluid Mech.* **148**, 451–460.

Miles, J. 1993 On Faraday waves. *J. Fluid Mech.* **248**, 671–683.

Miles, J. 1994 Faraday waves: rolls versus squares. *J. Fluid Mech.* **269**, 353–371.

Miles, J. & Henderson, D. 1990 Parmetrically forced surface waves. *Ann. Rev. Fluid Mech.* **22**, 143–165.

Ockendon, J. R. & Ockendon, H. 1973 Resonant surface waves. *J. Fluid Mech.* **59**, 397–413.

Pozrikidis, C. 1997 *Introduction to Theoretical and Computation Fluid Dynamics*. Oxford University Press.

Pozrikidis, C. 1998*a* *Numerical Computation in Science and Engineering*. Oxford University Press.

Pozrikidis, C. 1998*b* Gravity-driven flow of two adjacent layers through a channel and down a plane wall. *J. Fluid Mech.* **371**, 345–376.

Pozrikidis, C. 1999*a* Multi-film flow down an inclined plane: Simulations based on the lubrication approximation, and normal-mode decomposition of linear waves. In *Fluid Dynamics at Interfaces, Y. C. Yih Memorial Volume* (ed. W. Shyy). Cambridge University Press.

Pozrikidis, C. 1999*b* Theoretical and computational aspects of the motion of three-dimensional vortex sheets. *Submitted*.

Puckett, E. G. 1993 Vortex methods: an introduction and survey of selected research topics. In *Incompressible Computational Fluid Dynamics: Trends and Advances* (ed. M. D. Gunzburger & R. A. Nicolaides). Cambridge University Press.

Pullin, D. I. 1982 Numerical studies of surface-tension effects in nonlinear Kelvin–Helmholtz and Rayleigh–Taylor instability. *J. Fluid Mech.* **119**, 507–532.

Roberts, A. J. 1983 A stable and accurate numerical method to calculate the motion of a sharp interface between fluids. *IMA J. Appl. Maths* **131**, 13–35.

Schultz, W. W., Vanden-Broeck, J., Jiang, L. & Perlin, M. 1998 Highly nonlinear standing water waves with small capillary effect. *J. Fluid Mech.* **369**, 253–272.

Skalak, R. & Yarymovych, M. I. 1960 Forced large amplitude surface waves. *Proc. Fourth US Natl Congr. Appl. Mech.,* pp. 1411–1418.

Sorokin, V. I. 1957 The effects of fountain formation at the surface of a vertically oscillating liquid. *Sov. Phys. Acoust.* **3**, 281–295.

Wright, J. H. 1999 Numerical simulations of two-dimensional Faraday oscillations. Doctoral dissertation, Department of Mathematics, University of California, Berkeley.

Wu, J., Keolian, R. & Rudnick, I. 1984 Observation of a non-propagating hydrodynamic soliton. *Phys. Rev. Lett.* **52**, 1421–1424.

Zufiria, J. A. 1988 Vortex-in-cell simulation of bubble competition in a Rayleigh–Taylor instability. *Phys. Fluids* **31**, 3199–3212.